

2011-01-01

Ballistic Projectile Metallurgical Issues And Fundamentals: Aerosol Production In Rod Penetration Erosion And Erosion Phenomena Associated With Railgun Development

Brenda Ivette Machado

University of Texas at El Paso, bimachado@miners.utep.edu

Follow this and additional works at: https://digitalcommons.utep.edu/open_etd



Part of the [Materials Science and Engineering Commons](#), and the [Mechanics of Materials Commons](#)

Recommended Citation

Machado, Brenda Ivette, "Ballistic Projectile Metallurgical Issues And Fundamentals: Aerosol Production In Rod Penetration Erosion And Erosion Phenomena Associated With Railgun Development" (2011). *Open Access Theses & Dissertations*. 2331.
https://digitalcommons.utep.edu/open_etd/2331

This is brought to you for free and open access by DigitalCommons@UTEP. It has been accepted for inclusion in Open Access Theses & Dissertations by an authorized administrator of DigitalCommons@UTEP. For more information, please contact lweber@utep.edu.

BALLISTIC PROJECTILE METALLURGICAL ISSUES AND
FUNDAMENTALS: AEROSOL PRODUCTION IN ROD PENETRATION
EROSION AND EROSION PHENOMENA ASSOCIATED WITH RAILGUN
DEVELOPMENT

BRENDA I. MACHADO

Materials Science and Engineering

APPROVED:

Lawrence E. Murr, Ph.D., Chair

Stephen W. Stafford, Ph.D.

Kristine M. Garza, Ph.D.

Felicia S. Manciu, Ph.D.

Juan C. Noveron, Ph.D.

Benjamin Flores, Ph.D.
Acting Dean of the Graduate School

Copyright
by
Brenda I. Machado
2011

“Great teamwork is the only way we create the breakthroughs that define our careers.”
Pat Riley

BALLISTIC PROJECTILE METALLURGICAL ISSUES AND
FUNDAMENTALS: AEROSOL PRODUCTION IN ROD PENETRATION
EROSION AND EROSION PHENOMENA ASSOCIATED WITH RAILGUN
DEVELOPMENT

by

BRENDA I. MACHADO, M.S.

DISSERTATION

Presented to the Faculty of the Multidisciplinary Program
in Materials Science and Engineering of
The University of Texas at El Paso
in Partial Fulfillment
of the Requirements
for the Degree of

DOCTOR OF PHILOSOPHY

Materials Science and Engineering
THE UNIVERSITY OF TEXAS AT EL PASO

August 2011

Executive Summary

The issue is derived from ballistic erosion as it relates to nanoparticle production and respiration of these particles as a health concern ballistic erosion and ballistic erosion as it relates to railgun performance. A common thread between these two issues is dynamic recrystallization (DRX). DRX has been demonstrated to be the dominant mechanism for solid-state flow associated with ballistic projectile/target penetration and interaction, friction-stir welding phenomena, and other high-strain rate deformation phenomena. Friction and wear studies at lower strain rates and severe plastic deformation have also shown DRX to dominate surface-related microstructures, with variations in more conventional microstructures associated with plastic deformation with the stress-strain diagram (such as dislocations) decreasing with distance from the contacting surface(s).

This has been especially prominent for sliding friction and wear phenomena on copper surfaces which is the case of the railgun systems. Future US Navy ships will make significant advances in ship design, shipboard systems, and innovative weapon systems. One such weapon system is the electromagnetic rail gun which uses magnetic rails to launch a solid, non-explosive projectile at incredible speeds; they do not rely on chemical propellants like the kinetic energy projectiles. They promise to fire ammunitions ten or more times beyond conventional naval gun shells, while reducing both the required size of each shell and the amount of explosive material carried on board ship. Extremely long ranges, short time of flight and high lethality are three main war fighting objectives that are expected of these weapons. Due to the incredible speeds, the heat produce during launching, etc. the projectile and armature endure mechanical damage which is observed in the form of ballistic erosion by DRX.

In the case of the nanoparticle production both the target and the projectile erode by DRX which facilitates material flow in the solid state. This produces polycrystalline, millimeter, micron and submicron-size erosion and debris fragments from both the penetrating rod and the penetrated target, including some mechanical mixing and reaction product debris between the target and the projectile.

Health concerns come from the previous use of depleted uranium (DU) munitions especially in kinetic energy (KE) rod projectiles which have been historically associated with potential long-term health issues. The aerosolized particulates produced during an impact of depleted uranium munitions can potentially contaminate extensive areas around the impact sites and cause a wide spectrum of civilian and military health concerns. That is one of the main reasons that have prompted the consideration of alternative ballistic materials such as tungsten-heavy alloys (WHA). Kinetic energy rod projectiles made with tungsten alloys have historically been assumed to be relatively benign and to pose no health or environmental risks.

The assumption is based on the idea that the tungsten constituent of the alloy is non-toxic. A potential concern arises due to the presence of two toxic metals in the alloy, nickel and cobalt. Although they are in relatively small proportions, their presence raises a dilemma about risks associated with the inhalation and the ingestion of these metals. There has been recent studies that examined aerosols inside an armored vehicle penetrated by a KE rod penetrator and the aerosol data obtained serves as a quantitative foundation for future work in the area of health-risk assessments by eliminating some of the uncertainty surrounding possible exposures to aerosols during combat.

Table of Contents

Executive Summary	v
Table of Contents	vii
List of Tables	ixx
List of Figures	x
Chapter 1: Introduction	1
1.1 Kinetic Energy Penetrators	1
1.1.1 Aerosol Production	2
1.2 Railgun Erosion	3
1.3 Dynamic Recrystallization	3
1.4 References	4
Chapter 2: Previous Research	7
2.1 Characterization and Cytotoxic Assessment of Ballistic Aerosol Particulates for Tungsten Alloy Penetrators into Steel Target Plates	7
2.1.1 Materials and Ballistic Testing	7
2.1.2 Aerosol Collection and Analysis	8
2.1.3 <i>In-vitro</i> Cytotoxicity Assays for Particulate Collections	9
2.1.4 Observations/Summary	9
2.2 Investigations of Damage to Armature Railguns	11
2.2.1 Background	11
2.3 References	12
Chapter 3: Research Objectives	13
Chapter 4: Comparative Microstructures and Cytotoxicity Assays for Micron/Nano Metals Composing Ballistic Aerosols: The Respiratory Health Implications	15
4.1 Introduction	16
4.2 Materials and Methods	17
4.2.1 Ballistic Aerosol (Nanoparticulate) Production Methodology	17
4.2.2 Particulate Characterization	20
4.2.3 Cell Culture (Viability) Assays	20
4.3 Results and Discussion	21
4.3.1 Comparison of Manufactured Particulate Microstructures with Reference to Filter-	

Collected Ballistic Particulates	21
4.3.2 Viability Assays and Assay Comparisons	36
4.4 Conclusions.....	40
4.5 Acknowledgements.....	41
4.6 References.....	41
Chapter 5: Materials Characterization of Railgun Erosion Phenomena	44
5.1 Introduction.....	45
5.2 Experimental Details	47
5.3 Results and Discussion	50
5.4 Conclusions.....	62
5.5 Acknowledgements.....	63
5.6 References.....	64
Chapter 6: Summary and Conclusions	67
6.1 Summary.....	67
6.2 Specific Conclusions	67
Curriculum Vita	69

List of Tables

Table 2.1.1: Particulate Collection for WA #1 Impact Experiment	11
Table 4.3.1: Experimental (Manufactured) Powder Properties	36

List of Figures

Figure 1.1.1: Typical KE 120mm APFSDS-Tcartridge (sabot round) showing the complete assembly	2
Figure 1.1.2: Schematic view of rod and target impact at initial conditions, during, and after penetration	2
Figure 1.3.1: DRX involvement in projectile/target penetration and high-strain rate deformation phenomena.....	4
Figure 2.1.1: Ballistic aerosol particulate generation and collection. The sabot-fired KE rod penetrates 10 mild steel target plates in an RHA cube confinement. A cascade impactor or single-filter collector collects particulates from the debris fields in separate penetration events	8
Figure 4.2.1: Ballistic projectile, kinetic energy rod penetration of a target plate. (a) Rod of length, l_0 , impacting a plate at a velocity of u_0 . (b) Penetrating rod, eroding at its head to form a rod erosion tube (RET) around the projectile head at reduced velocity u_0' . (c) Perforated plate which has formed a target erosion tube (TET) similar to the RET in (b). Ballistic debris field in the front and rear of the impacted target (D). (d) Polished cross-section of a 3.5 cm Cu target plate penetrated by a WHA rod. (e) Flash X-ray radiograph showing WHA rod penetrating the Cu target in (d). The eroded projectile head exiting the target is shown at P. The debris field behind target plate is shown at D. (d) and (e) are from Kennedy and Murr (2002)	18
Figure 4.2.2: Section view of polished and etched W-(KE) rod penetrating a steel target plate at an impact velocity (u_0 in Figure 4.2.1) of 1.3 km/s. Note TET and RET zones which flow in the direction opposite to the penetration direction. Debris fragments are denoted D. Also note recrystallization of the head of the single-crystal W rod, and erosive flow at the head	19
Figure 4.3.1: FESEM view of collected ballistic (impact) debris (a), and the corresponding EDS spectrum (b): W-Ni-Fe	22
Figure 4.3.2: TEM image of collected impact debris as in Figure 3(a), (a) and corresponding EDS spectrum (b): W-Ni-Fe. Note the sandwich is composed of coated Cu grids. The Cu peak ($K\alpha$) arises from the grid. Note small Ni peak	23
Figure 4.3.3: TEM X-ray (EDS) mapping sequence for W-Ni-Fe ballistic debris sample. (a) Bright-field image of aggregated particulates. (b) W map. (c) Ni map. (d) Fe map	24
Figure 4.3.4: TEM X-ray (EDS) mapping sequence for W-Ni-Co ballistic debris sample. (a) Bright-field image of aggregated particulates. (b) EDS spectrum of (a). (c) Ni map. (d) W map. (e) Fe (f) Co map	25
Figure 4.3.5: FESEM images of Fe and W micron-size powders. (a) Fe (ESPI, Inc.). (b) Fe (Aldrich). (c) W (Buffalo Tungsten, Inc.)	27
Figure 4.3.6: Magnified FESEM images for Fe and W micron-size powders. (a) Fe (Aldrich). (b) W	28

Figure 4.3.7: TEM image for nano-Fe powder with FESEM image insert showing nanoparticulate aggregation	29
Figure 4.3.8: TEM image for nano-W powder with FESEM image insert showing nanoparticulate aggregation	30
Figure 4.3.9: FESEM images for Ni (a) and Co (b) micron-size powders	31
Figure 4.3.10: TEM image for nano-Ni powder with FESEM insert showing nanoparticulate aggregation. The features noted by arrows are microstructural twins in the particles	32
Figure 4.3.11: TEM bright-field (a) and dark-field (b) sequence for nano-Ni powder utilizing selected diffraction spots from the selected-area electron diffraction pattern insert (circle). Arrows in (b) show diffracting nanoparticles	33
Figure 4.3.12: TEM image for nano-Co powder with FESEM insert showing nanoparticulate aggregation	34
Figure 4.3.11: High resolution TEM image for nano-Co powder aggregates showing Moire fringe pattern with 1.3 nm fringe spacing (arrow)	35
Figure 4.3.14: Comparative cytotoxicities (as relative A549 epithelial cell viability). (a) and (b) show collections for 4 separate ballistic events: 2 for W-Ni-Fe and 2 for W-Ni-Co KE rods penetrating Fe target plates. (c) and (d) compare nano and micron-size powders at concentrations in culture of 10 $\mu\text{g/mL}$. (e) and (f) compare nano and micron-size powders at concentrations in culture of 5 $\mu\text{g/mL}$. (g) and (h) compare nano and micron-size powders at concentrations of 2.5 $\mu\text{g/mL}$. All cell culture assays ((a) to (h)) are compared to culture media as a control. (a) and (b) also show blank filter culture as a control. (c) to (h) show DMSO as a control. Key note: $p < 0.5 = *$, $p < 0.0015 = **$, $p < 0.0001 = ***$	37
Figure 5.1.1: Schematic view for railgun principles. Current (I) flowing through rails and armature produces surrounding magnetic flux. Armature field interaction with rail flux creates force (F) on the projectile	46
Figure 5.1.2: Section and cut-away view for a railgun system showing armature, rail, and insulator layout in present experiments (after ref. 5). Rail damage on extracted copper rail section is illustrated. Note section reversal. Rail grooving damage occurs at the rail edges. Also note that current, field, and projectile force components are the same as in Fig. 5.1.1	46
Figure 5.2.1: Examples of left and right (A and B) extracted rail sections as in Fig. 5.1.2 at distances noted (4, 12, and 30 inches (x 2.54 cm/in.). Samples 4B and 12B were examined in detail in this research program. The surface section microindentation hardnesses are shown in the 4B specimen (lower right). Dotted circular enclosures illustrate sample extraction for TEM analysis. 1 refers to electro thinning from the copper side to view through the Al/Cu interface; 2 refers to a region for FIB extraction in order to observe the Al/Cu interface simultaneously (normal to the view for 1)	48
Figure 5.3.1: 3-D optical metallographic composite showing copper rail grain structure to be characterized by thin, irregular pancaked grains	51

Figure 5.3.2: Al and Cu zone structures in 12B sample (Fig. 3). (a) Porous Al deposit. (b) Scratched Cu rail surface portion. Secondary electron images	52
Figure 5.3.3: Low (a) and higher (b) magnification views for porous (gas bubble) structure in Al-alloy projectile, tribomaterial deposit on Cu rail (12B in Fig. 3). Secondary electron images	53
Figure 5.3.4: SEM views showing porosity (gas bubble) variations along the edge of the Al-alloy deposit on the Cu rail. (a) High porosity; (b) low porosity. From sample 4B in Fig.5.2.1	54
Figure 5.3.5: Corresponding TEM images for thin foil sections representing the Al/Cu interfacial region. (a) Mixing of Cu crystalline grains (arrows) within the Al matrix. (b) crystalline/amorphous mixing: Cu grains in essentially amorphous Al matrix	55
Figure 5.3.6: High-resolution TEM images of Al/Cu interfacial region (12B in Fig. 3) showing Moiré fringe, crystalline features intermixed with amorphous matrix. (a) Low magnification image, (b) higher magnification image	56
Figure 5.3.7: High-resolution TEM image for crystalline grain showing dislocations (arrow). The dashed-line enclosure represents a reference area 25 nm on a side (625 nm^2).....	57
Figure 5.3.8: Near-surface Cu rail microstructure observed in the TEM. The double diffraction spots in the SAED pattern insert attest to the 11° misorientation of the grain boundary. The superimposed patterns for A and B grains each have a (112) surface orientation.....	58
Figure 5.3.9: FIB-prepared and mounted Al/Cu interface section from Fig. 3 (sample 12B). The large arrow in the magnified, TEM-image insert indicates a specific area examined.....	59
Figure 5.3.10: TEM bright-field image of interfacial Al/Cu region marked by large arrow in Fig. 5.3.9	60
Figure 5.3.11: TEM mapping sequence for the Al/Cu interface in Fig. 13. (a) Al map and (b) Cu map.	60
Figure 5.3.12: Magnified TEM images corresponding to Al and Cu regions in Fig. 14 somewhat removed from the interfacial (transitional) region. The SAED pattern insert in the Cu region shows an (fcc) ring pattern	61

Chapter 1: Introduction

The goal of this research was to characterize and compare ballistic particulates collected during rod penetration events as well as to explore the fundamental microstructural issues associated with aluminum armature-projectile and copper-rail degradation. A common thread between these two issues is dynamic recrystallization (DRX) as these particulates erode. The following sections give a brief introduction to better help understand the formation of these erosion particulates by the two different ballistic methods and how they connect to this common thread of DRX. Section one gives background information on kinetic energy (KE) penetrators and how aerosol is produced. Section two provides fundamental information on railgun systems. Lastly, section three illustrates a correlation between the eroded particulates in rod penetration and railgun erosion phenomena to DRX.

1.1 Kinetic Energy Penetrators

KEPs are projectile weapons that do not explode, but rather damage their target by hitting into it at high speeds ($\approx 1.4 - 1.9$ km/sec) through the use of kinetic energy from high pressure gases that are generated by the burning of propellant in a barrel rather than from an explosive source (Murr and Pizaña 2007). Also, it relies on mass (density) to effectively pierce the armor and destroy the target. These types of projectiles have a higher length to diameter ratio and are referred to as “long rod penetrator” (refer to Figure 1.1.1). It is composed of two assemblies, a combustible case and propellant assembly, and the sabot and sub-caliber projectile assembly (Murr and Pizaña 2007). The propellant and fuse assembly supplies the kinetic energy to the sabot and sub-caliber projectile assembly. When the projectile assembly is ejected from the barrel the high drag pulls the sabot quickly away from the long rod projectile, thereby allowing for a straight trajectory stabilizing the projectile.



Figure 1.1.1: Typical KE 120mm APFSDS-Tcartridge (sabot round) showing the complete assembly [2].

1.1.1 Background on Aerosol Production

Ultra-fine or nano-particulates with various morphologies and chemistries exhibit varying degrees of respiratory toxicity as determined by several cytotoxicity (*in-vitro*), cell-culture studies (Donaldson et al 2001; Pope III et al 2006; Soto et al 2008; and Murr et al 2008) . Several of these atmospheric particulates or aerosol compositions in excess of 1 μm do not usually exhibit any detectable cytotoxicity (Donaldson et al 2001; Pope III et al 2006; and Pizaña et al 2006). When using KE projectiles through thick metal or alloy targets both the both target and rod erosion produced aerosol debris outflow from the entrance side of the target, concluded by the formation of a rear debris field when the projectile exits the target upon perforation as shown in Fig. 1.2.1 (Oberdörser 2001; Kalinich et al 2005; Pappu et al 1999; Kennedy et al 2002; Carleone 1993; Trillo et al 2002; Pappu et al 2001; and Murr et al 2002).

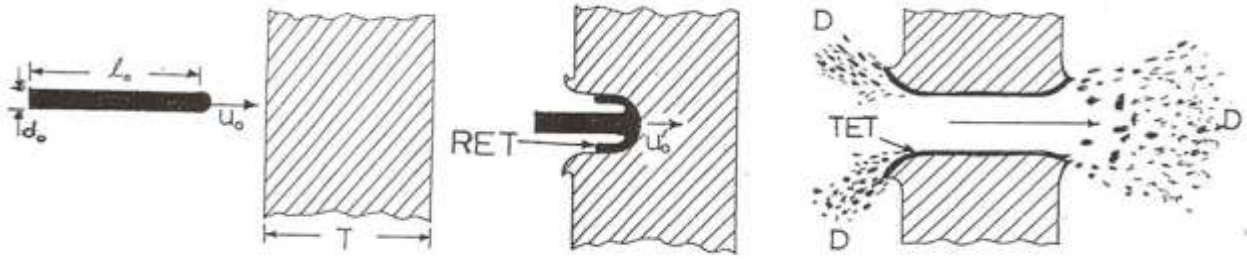


Figure 1.1.2: Schematic view of rod and target impact at initial conditions, during, and after penetration [15].

1.2 Railgun Erosion

Optimum parameters are desirable on railgun systems to make the most of their life. For example, the accelerating force between the rails and armature depends on the magnetic field present and is obtained by changing several variables in the railgun design like the current through the rails. Very high currents are employed to accelerate the armature which produces areas of large energy and resistive heating on the rail. The rail is also in contact with the armature which causes rail (ballistic) erosion and results in a major limitation to railgun performance. Railgun erosion is currently the main issue restricting their use as other category in military armaments. By studying the erosion caused under different conditions it may be possible to determine a solution to maximize rail life.

1.3 Dynamic Recrystallization

The interaction between the rod and the projectile or in the case of the railgun systems between the rail and the armature involves a solid-state flow/erosion. Dynamic recrystallization is the principal mechanism for solid state-flow as stated previously. Figure 1.3.1 shows a schematic on how DRX is involved in the process of both rod penetration erosion and erosion phenomena in railgun development. The projectile aerosol erosion by DRX creates a rod erosion tube (RET) that is ejected from the rear of the projectile and a target erosion tube (TET) ejected in the same direction forming the target crater rim and the related debris particulates as shown in Figure 1.1.1 (a) and (b). There is a possibility of a

reaction or interaction between the projectile and the target, and there may also be some local melt and solidification phenomena (Pizaña 2006). Figure 1.1.1 (c) suggests the formation of erosion deposits on the surface by DRX as the armature slides through the rail at high strain rates.

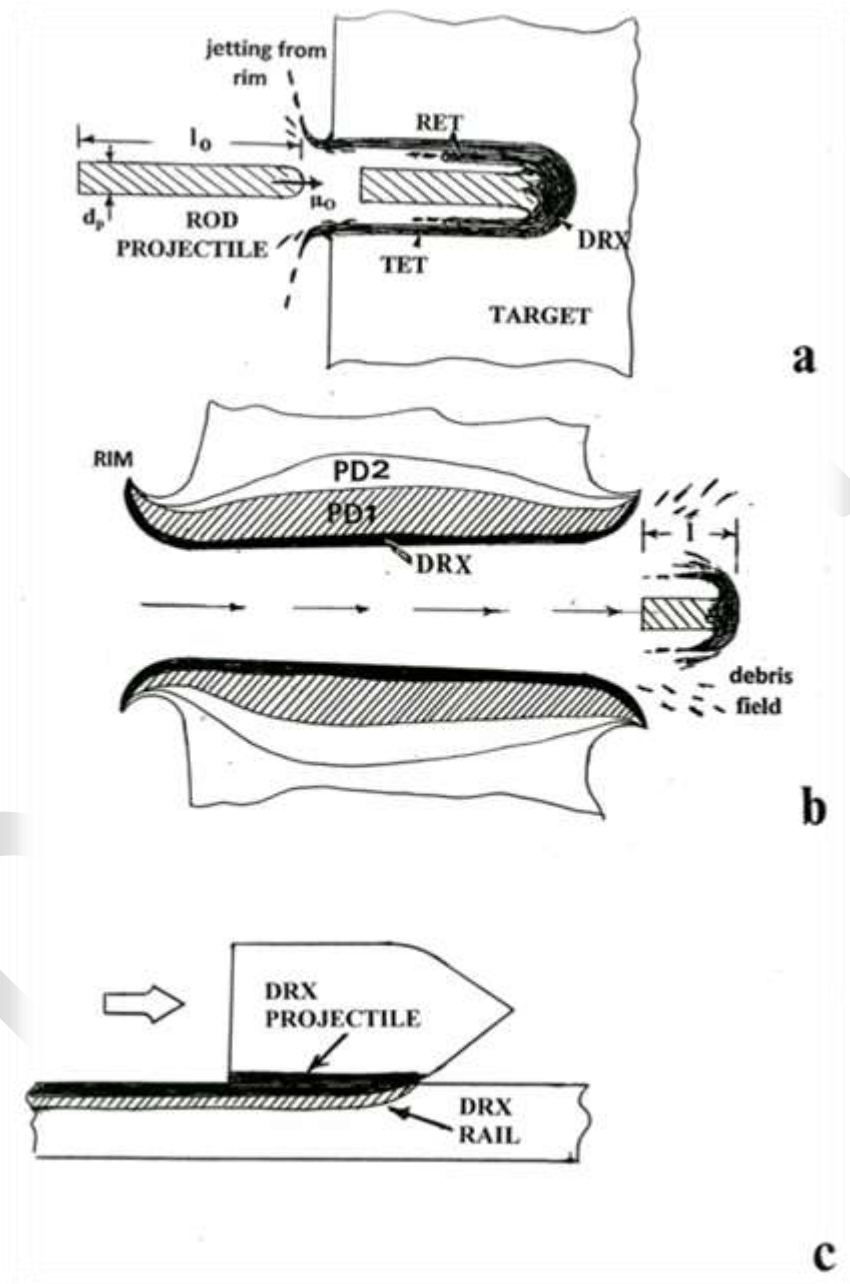


Figure 2.1.3: DRX involvement in projectile/target penetration and high-strain rate deformation phenomena.

1.4 References

- Carleone, J. 1993. Tactical missile warheads: progress in astronautics and aeronautics. American Institute of Aeronautics and Astronautics Inc. Vol. 155: Washington, DC.
- Donaldson, K., Stone, V., Clouter A, et al. 2001. Ultrafine particles. *Occup. Environ Med*, 58:211-15.
- Kalinich, F.; Emand, C.A.; Dalton, T.K.; et al. 2005. Embedded Weapons-Grade Tungsten Alloy Shrapnel Rapidly Induces Metastatic High-Grade Rhabdomyosarcomas in F344 Rats. *Environ. Health Perspect.* 113: 729-731.
- Kennedy, C.; Murr, L.E. 2002. Comparison of tungsten heavy-alloy rod penetration into ductile and hard metal targets: microstructural analysis and computer simulations. *Mater. Sci. Eng.* A325: 131-143.
- Murr, L.E., , C. 2007. Dynamic recrystallization: the dynamic deformation regime. *Metall. & Mater. Trans*, 38A: 2611-2628.
- Murr L.E., Soto K.F., Garza K.M., 2008. Health hazards of manufactured, natural environmental and anthropogenic atmospheric nanoparticulate materials: Past, present and future. In Chapter 1 *Biomaterial and Biomedical Engineering*, ed. A. Oechsner A, 1-54. trans. Tech Publishers: Switzerland.
- Murr, L.E., Trillo E.A., Pappu S., Kennedy C. 2002. Adiabatic shear bands and examples of their role in severe plastic deformation. *J. Mater. Sci.* 37: 3337-3390.
- Oberdörser G, 2001. Pulmonary effects of inhaled ultrafine particles. *Int. Arch. Occupat. Environ. Health*, 74: 1-8.
- Pappu, S., Kennedy, C., Murr, L.E., Magness, L.S., Kapoor D. 1999. Microstructure analysis and comparison of tungsten alloy rod and [001] oriented, columnar-grained tungsten rod ballistic penetrators. *Mater. Sci. Eng.* A262: 115-128.

- Pappu, S., Sen, S., Murr, L.E., Kapoor, D., Magness, L.S. 2001. Deformation twins in oriented, columnar-grained tungsten rod ballistic penetrators. *Mater. Sci. Eng.* A298: 144-157.
- Pope III, C.A., Dockery, D.W. 2006. Health effects of particulate air pollution: lines that connect. *J. Air & Waste Manage. Assoc.*, 56: 709-742.
- , C., Mu .Y., Tamoria, T.L., Chen H.C., Cytron, S.T. 2006. Solid-state flow, mechanical alloying, and melt-related phenomena for [001], single-crystal w ballistic rod penetrators interacting with steel targets. *Mater. Sci. Eng.* A428: 301-313.
- Soto K.F., et al. 2008. Direct contact cytotoxicity assays for filter-collected, carbonaceous (dust) nanoparticulate. Material and observations of lung cell response. *Atmos Environ*, 42: 1970-82.
- Trillo, E. A.; Esquivel, E.V.; Murr, L.E.; Magness, L.S. 2002. Dynamic recrystallization induced flow phenomena in tungsten-tantalum (4%) [001] single-crystal rod ballistic penetrators. *Matls. Charac.* 48: 407-421.

Chapter 2: Previous Research

The following two sections provide some background on the specific issues studied in this dissertation. They provide a justification for the supplementary examination of these areas that were considered for further observation and analysis.

2.1 Characterization and Cytotoxic Assessment of Ballistic Aerosol Particulates for Tungsten Alloy Penetrators into Steel Target Plates

This study was concerned with the systematic collection of aerosol particulates associated with ballistic WHA rod penetration into rolled homogeneous steel or related steel armor or armor plate sequences. As well as with the characterization of these collected particulates and finally lung human epithelial cells were exposed to nanoparticles contained within filters to assess their inflammatory and related respiratory health effects.

2.1.1 Materials and Ballistic Testing

Sub-scale WHA penetrators were fired into an array of mild steel plates which were encapsulated in a steel containment vessel. The penetrators were hemispherical-nose, 65 g rods with a length to diameter ratio of 20. The WHA rods consisted of either 91% (by weight) W, 5.6% Ni, 1.4% (WA #1) or 92% W, 6% Ni, 3% Co (WA #2) or and were fabricated using liquid phase sintering (German 1985, 251).

The target array consisted of 10 each of 6.25 mm thick mild steel plates spaced 12.5 mm apart backed by a thick RHA block to capture the residual penetrator. The penetrators were fired from a 26 mm smooth bore cannon outfitted with a 37 mm breach. The launch package consisted of a polypropulux laboratory sabot and obdurator with a steel pusher plate. The penetrators (and entire launch package) were fired at a velocity of ~ 1.2 km/s using approximately 170 g of type M2 propellant, which is mainly composed of nitrocellulose. In all 12 tests, the penetrators completely perforated all of the thin mild steel plates and were caught in the thick RHA block.

The containment vessel was an RHA cube with a wall thickness of ~25 mm, with an internal open volume that was approximately 60 cm on a side. This vessel had a removable top which allowed for placement of the target array. The vessel had two ports: a ~10 cm diameter port through which the WHA penetrators were fired and a smaller ~6 mm port to allow for aerosol sampling. This containment vessel is not a closed system as the larger port is open during the ballistic test and throughout the sampling period. In Fig 2, we show a representative schematic of the ballistic test set-up including the penetrator launch package, mild steel target array and containment vessel.

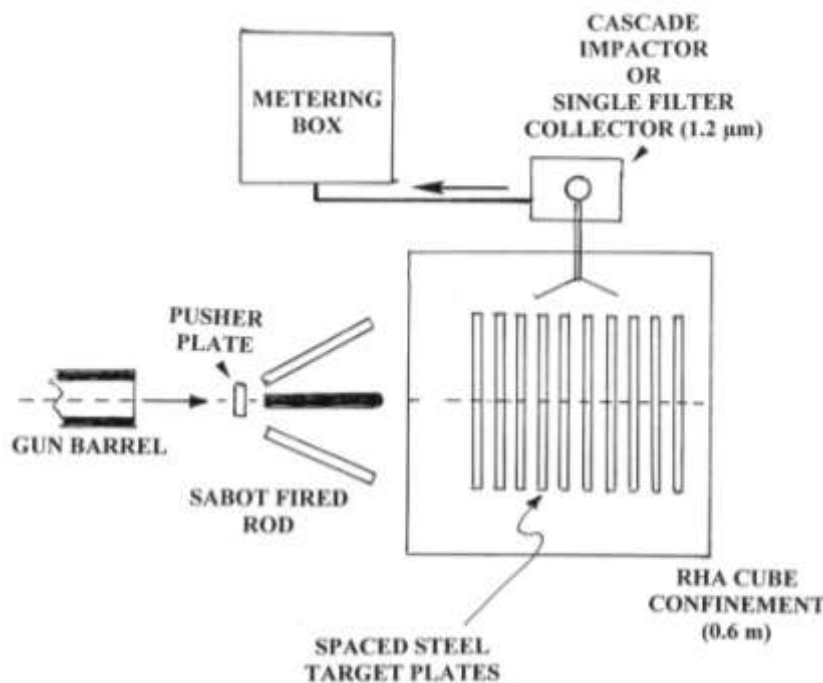


Figure 3.1.1: Ballistic aerosol particulate generation and collection. The sabot-fired KE rod penetrates 10 mild steel target plates in an RHA cube confinement. A cascade impactor or single-filter collector collects particulates from the debris fields in separate penetration events.

2.1.2 Aerosol Collection and Analysis

Immediately following the ballistic test, aerosol samples were collected using either single-stage filters or by an eight-stage cascade impactor. The debris (particulate aerosol) generated by the rod impact, penetration and perforation as well as the residual propellant gases were sampled for ~15 minutes through the respective collection media with an airflow rate of 2 L/min.

The single stage filters were SKC model 225-321A mixed cellulose ester (MCE) filters with a diameter of 25 mm and a pore-size of 0.8 μm . The eight stage cascade impactor utilized Mylar substrates with cut-points ranging from 0.5 to 21 μm and with a final backup filter with a 0.25 μm pore size. The Mylar substrates were sprayed with Dow Corning 316 silicone release lubricant ~16h before initial weighing to provide an adhesive surface for the airborne particles. The total particulate concentrations at each cut point were determined from gravimetric analysis.

2.1.3 *In-vitro* Cytotoxicity Assays for Particulate Collections

Direct contact assays were performed using collected ballistic particulates using the single-stage filters (SSF) associated with ballistic impact of WA #1 and WA #2. Assays were performed for both single stage filters as well as for the cascade impactors for the two groups (WA #1 and WA #2). Untreated cells (or “media” only cells) served as the negative control; cells exposed to a filter on which nothing had been collected served as the blank control. These assays measure *in vitro* cell viability or cell death using colorimetric or optical densitometry analysis along with cytokine enzyme linked immuno sorbent assay (ELISA) studies which measure the up-regulation and release of interleukins by the cells.

As in many recent ELISA studies, we utilized the immortalized A549 human epithelial lung cell line which provides an effective *in vitro* lung cell model. This colorimetric assay assesses relative viability as a function of color, which is directly proportional to the amount of cells available to convert the substrate into a color product. These type of epithelial cells have the ability to synthesize and release inflammatory cytokines such as Interleukin (IL)-6 and IL-8, which are considered markers for inflammatory response associated with allergic responses and pulmonary diseases.

2.1.4 Observations/Summary

As in the case for environmental particulate regimes, including the outdoor environment, nanoparticulates accounted for the most significant number concentration or particulate abundance of

the ballistic aerosol, with mass abundances exceeding 150 mg/m^3 (Table 2.1.1). Correspondingly, these small mass abundance values represented the most cytotoxic aerosol category in contrast to larger concentrations of other soot species. In this work, ballistic aerosol composed largely of nanoparticulates averaging $\sim 10 \text{ nm}$ was shown to be highly toxic to human epithelial cells over a short time (48 h) in culture that the cells died before they could produce any responsive cytokines (IL-6 or IL-8). Lower ballistic aerosol concentrations measured to be roughly $\frac{1}{4}$ of the topic concentrations showed no measurable cell (A549 human epithelial) death after 48 h in culture. While the concentration cut off and exposure time in culture to affect significant epithelial cell death was not determined, the aerosol characterization and cytotoxicity assays provide compelling evidence for significant health hazards “for exposure, inhalation, and respiration of aerosolized metals” as earlier suggested by Gold et al. (2007) for military crew compartment armor steel perforation by a WHA-KE penetrator of the type studied in this work.

Although the nanoparticulate species or stoichiometries contributing significantly to epithelial cell death were not fully characterized, considerable quantities (concentrations) of iron oxides and other metal or metal oxide nanoparticles contribute significantly to the ballistic aerosol and these have already been demonstrated to be highly cytotoxic. It is also not known how these various nanoparticle species contribute synergistically to the highly toxic behavior of the ballistic aerosol. Despite these shortcomings, this research suggests that there is the potential for severe or chronic respiratory health effects associated with even short-term exposure to ballistic aerosol at high concentrations associated with KE penetrator perforation of crew compartments in a variety of armored vehicles. Current research reviews indicate that with few exceptions, nanoparticles and nanoparticle aggregates are toxic (if not cytotoxic) to living organisms (Buzca et al 2007 and Murr et al 2008). However, the relationship between nanoparticle exposure and immune response is not well known. The degree of toxicity for

specific nanoparticles cannot be extrapolated from bulk properties, and materials which are nontoxic in bulk form may be toxic in nanoparticle or nanoparticle aggregate form (Buzca 2007).

Table 2.1.1: Particulate collection for WA #1 impact experiment

Stage	Cut Point (microns)	Total Particulate Weight (mg)	Total Particulate Concentration (mg/m ³)	Iron Conc. (mg/m ³)	Nickel Conc. (mg/m ³)	Tungsten Conc. (mg/m ³)
1	21	0.432	17	14.8	0.286	1.92
2	15	0.052	2	4.51	0.134	1.36
3	10	0.000	0	3.52	ND	0.217
4	6	0.049	2	7.31	0.118	0.318
5	3.5	0.798	31	21.0	0.312	0.736
6	2	0.953	38	20.9	0.290	0.781
7	0.9	0.677	27	9.97	0.142	0.625
8	0.5	0.204	8	2.25	ND	0.401
Backup Filter	0.25	0.878	35	4.89	ND	2.59
Total			160	89.2	1.28	8.95
Respirable			106	65.0	0.862	3.08

ND – Concentration below instrument detection limit

2.2 Investigations of Damage to Armature Railgun Systems

The life of solid armature railguns is a critical issue that has led to several experiments. Previous research has been done on railgun systems to investigate their mechanism, the sliding contact between the rails and the armature, but most importantly the damage observed on the rails.

2.2.1 Background

Over several years the Institute for Advanced Technology (IAT) has investigated the design of railgun systems and tested a series of subscale railgun configurations. Damage to rails in solid-armature railguns can be due to mechanical deformation and melting as well as liquid and plasma erosion. Some of the damage observed happens in the startup region where grooving is observed. In 1998 grooving was first observed by Gee and Persad (2001), who evaluated several materials as candidates for use in the startup region of the rails (Gee and Persad 2001). It was again observed by the IAT after multishot tests were performed with an aluminum alloy armature and rail.

To study the progression of this type of damage on the rail, multishot experiments were conducted with copper rails, G-10 insulators, and an aluminum armature. This type of damage to the rail is not wanted in the process because it degrades not only the material in the rail, but the design in general and generates unbalance forces that can destabilize the launch pack.

2.2.3 References

- Buzca C., Pacheco, J., Robbie, K. 2007. Nanomaterials and nanoparticles: sources and toxicity. *Biointerphases* (2): 17-71.
- Gee, R. M. and C. Persad. 2001. The response of different copper alloys as rail contacts at the breech of an electromagnetic launcher. *IEEE Trans. Magn.* (37)1: 263.
- German, R. M. 1985. *Liquid phase sintering*, 251, New York, NY: Plenum Press.
- Gold, K., Cheng, Y.S., Holmes, T.D. 2007. A quantitative analysis of aerosols inside an armored vehicle perforated by a kinetic energy penetrator containing tungsten, nickel, and cobalt. *Military Med.* 172 (4): 393-398.
- Murr, L.E., Soto, K.F., Garza, K.M. 2008. Health hazards of manufactured, natural environmental and other anthropogenic atmospheric nanoparticulate materials: past, present and future. In *Biomaterials and Biomedical Eng.*, eds. W. Ahmed and N. Ali, 1-55, trans. Tech Publishing: Switzerland.

Chapter 3: Research Objectives

The main goal of this research was to study the ballistic metallurgical issues and fundamentals of the aerosol erosion production in rod penetration and the erosion phenomena associated with railgun development. The two related ballistic nano-particle issues involve speciated nano-particles of W, Ni, Co, and Fe representing ballistic aerosol examined for human toxicity in comparison to related ballistic aerosol and railgun erosion of nanoparticulates to be examined and characterized relative to railgun degradation issues.

In the previous study presented in Chapter 2 we were concerned with the systematic collection of aerosol particulates associated with ballistic WHA rod penetration into rolled homogeneous (steel) armor (RHA) and this study was an effort to compare commercial micron and nano-sized particles of Fe, W, Ni, and Co to the original collection of aerosol particulates. In exploring the fundamental microstructural issues associated with aluminum armature-projectile and copper rail degradation we concentrated on projectile erosion and deposition upon the rail system. This would be in contrast to the study of erosion particulates created during ballistic rod penetration.

The specific objectives of this research include the following:

1. Fully characterize the distribution of aggregates and identify the specific location of the metals in the alloy.
2. Examine the cytotoxicity results if any on the different particles for the different mixtures of W/Fe, W/Ni, W/Co, Fe/Ni, Fe/Co, therefore completing previous research (Machado, et al. 2010).
3. Confirm if the nano particles are indeed toxic in comparison to micron-size particles as well as their morphologies.

4. Fully characterize aluminum projectile wear debris and the interface between aluminum wear debris coatings and the copper rails in order to address the degradation/wear mechanism and determine potential alternative materials systems.

The first objective analyzes the distribution of the specific metals to identify how they are distributed in comparison to the complete aggregate. The second and third objective examine the mixtures of the same metals as in the original ballistic filters which try to simulate the original concentrations and determine if these blends could be toxic. The fourth objective evaluates the projectile erosion and deposition upon the rail system of nanoparticles that could also present a possible health hazard. Overall, these objectives will help advance in understanding some fundamental ballistic metallurgical issues that are required for an effective railgun system material and also in the health effects (if any) that could be produced by the distribution of the different metal mixtures.

Chapter 4: Comparative Microstructures and Cytotoxicity Assays for Micron/Nano Metals Composing Ballistic Aerosols: The Respiratory Health Implications

The material of this chapter has been recently published in the International Journal of Nanomedicine under manuscript ID # 15537

Abstract

Aerosol particulates collected on filters from ballistic penetration and erosion events for W-Ni-Co and W-Ni-Fe kinetic energy rod projectiles penetrating steel target plates were observed to be highly cytotoxic after 48 h exposure to human epithelial A549 lung cells in culture. The aerosol consisted of micron-size Fe particulates and considerable nanoparticulate aggregates consisting of W, Ni or W, Co and some Fe, characterized by SEM and TEM, and using energy-dispersive (X-ray) spectrometry by (EDS) for elemental analysis and mapping. Cytotoxic assays of micron-size and nano-size, manufactured metal particulates of W, Ni, Fe, and Co demonstrated that, consistent with extensive literature studies, that only the nanoparticulate elements demonstrated measurable cytotoxicity. These results suggest very severe, short-term, human toxicity especially related to respiratory health implications on breathing ballistic aerosols.

4 Comparative Microstructures and Cytotoxicity Assays for Micron/Nano Metals Composing Ballistic Aerosols: The Respiratory Health Implications

B. I. Machado, R. Suro, K. M. Garza, L. E. Murr

4.1 Introduction

It is now well established that ultra-fine or nano-particulates with a wide range of morphologies and chemistries exhibit varying degrees of respiratory toxicity as determined by cytotoxicity (*in-vitro*), cell-culture assays (Donaldson et al 2001; Murr et al 2008; Pope and Dockery 2006; Soto et al 2005). Correspondingly, atmospheric particulates or aerosol compositions in excess of 1 μm for the same dose do not usually exhibit any detectable cytotoxicity (Donaldson et al 2001; Oberdörster 2001; Pope and Dockery 2006).

A recent study by Machado et al (2010) involving filter collections representing aerosol debris resulting from tungsten heavy alloy (WHA), kinetic energy (KE) rod projectiles penetrating steel plate arrays in steel enclosure demonstrated the induction of rapid and complete death of a human epithelial cell type in culture. This suggests that there may be a severe human toxicity potential for inhaled ballistic aerosol inside an armored vehicle penetrated by a variety of projectiles, particularly WHA rods into steel armor.

Earlier work by Guillmette et al (2006) addressed the potential health risks for depleted uranium (DU) aerosols, while Gold et al (2007) also examined aerosols inside an armored vehicle penetrated by WHA projectiles. While Gold et al (2007) and Machado et al (2010) detected a variety of ultra-fine (nano) and fine (micron) sized particulates, only the work by Machado et al (2010) demonstrated severe respiratory health prospects, although there was no clear indication of the specific role played by nanoparticulates in contrast to fine, micron-size particulates, or chemical speciation effects, if any. Machado et al (2010) demonstrated a propensity for Fe particles (ranging from $\sim 1 \mu\text{m}$ to $0.01 \mu\text{m}$) as well as smaller W particulates ($< 1 \mu\text{m}$). There was no indication of elemental mixing of the target and

WHA (Fe and W, respectively). Although the projectiles also contained ~8% (weight) of either Fe and Ni, or Fe and Co, there was no significant evidence for these elements either in combined (or alloyed) form or as single-component nanoparticulates in the collected aerosol, even though the nanoparticulate fraction collected on filters dominated the particle concentration.

In the present study, we performed cell culture assays using a human epithelial (lung model) cell line for micron and nano-sized particles of Fe, W, Ni, and Co after careful characterization by both scanning and transmission electron microscopy. In addition, we performed energy-dispersive X-ray analysis and high-resolution elemental mapping of previously collected aerosol particles scraped from collection filters in order to establish the elemental compositions (chemistries) for a wide distribution of collected particulates, particularly nanoparticulates, for comparison with the speciated particulates by comparison of the prior cell culture assay results (Machado et al 2010) with those for speciated particulates. Finally, we mixed speciated nanoparticulates (Fe/W; W/Ni, W/Co Fe/Ni; Fe/Co, etc.) and examined their cytotoxicity in contrast to the original filter assays, as well as the single-element particulates in the context of symbiotic effects for mixed chemistries; especially for the collected nanoparticulates.

4.2 Materials and Methods

4.2.1 Ballistic Aerosol (Nanoparticulate) Production Methodology

Figures 4.2.1 and 4.2.2 are intended to provide a fundamental overview of debris generation during the penetration and perforation of a KE rod into a steel target or targets. Beginning with Figure 4.2.1a to c, the penetration process is illustrated schematically. As the KE rod, with initial length l_0 (Figure 4.2.1a), penetrates the target (Figure 4.2.1b), both the target and projectile erode, with target material effectively flowing backward (opposite to the projectile penetration direction) along with the erosion products from the penetrator which are referred to as a rod erosion tube (RET) streaming from the head of the penetrating projectile rod. The target also erodes or excavates as a target erosion tube

(TET in Figure 4.2.1c) where upon perforation of the target as illustrated in Figure 4.2.1c produces a debris field consisting of aerosol particulates at the back of the target indicated by D in Figure 4.2.1c. Figure 4.2.1d and e illustrate this phenomena for the penetration (and perforation) of a WHA rod into a copper target. Figure 4.2.1d shows a half-section for the penetrated target while Figure 4.2.1e illustrates a flash X-ray image for the eroded rod projectile exiting the target at P. The X-ray radiograph also captures the debris field production (D) at the back of the target.

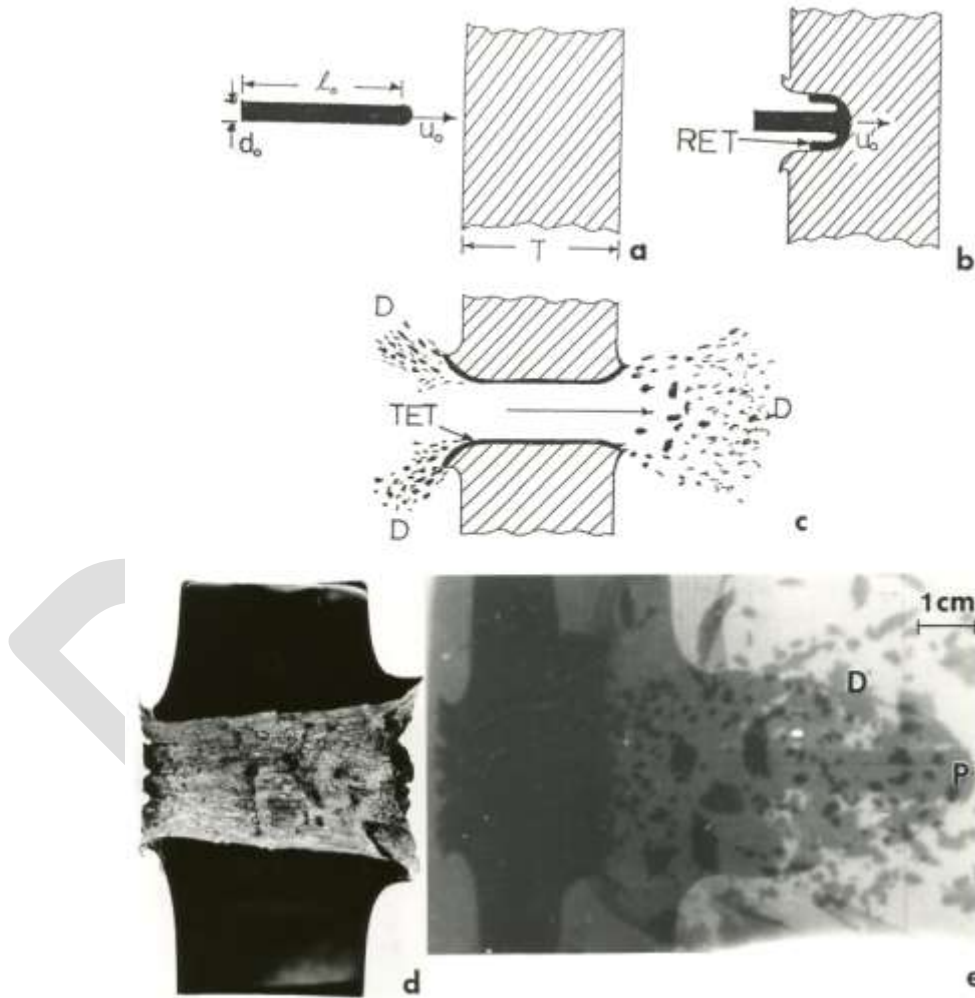


Figure 4.2.1: Ballistic projectile, kinetic energy rod penetration of a target plate. (a) Rod of length, l_0 , impacting a plate at a velocity of u_0 . (b) Penetrating rod, eroding at its head to form a rod erosion tube (RET) around the projectile head at reduced velocity u_0' . (c) Perforated plate which has formed a target erosion tube (TET) similar to the RET in (b). Ballistic debris field in the front and rear of the impacted target (D). (d) Polished cross-section of a 3.5 cm Cu target plate penetrated by a WHA rod. (e) Flash X-ray radiograph showing WHA rod penetrating the Cu target in (d). The eroded projectile head exiting the target is shown at P. The debris field behind target plate is shown at D. (d) and (e) are from Kennedy and Murr (2002).



Figure 4.2.2: Section view of polished and etched W-(KE) rod penetrating a steel target plate at an impact velocity (u_0 in Figure 4.2.1) of 1.3 km/s. Note TET and RET zones which flow in the direction opposite to the penetration direction. Debris fragments are denoted D. Also note recrystallization of the head of the single-crystal W rod, and erosive flow at the head.

As described in detail by Pizaña et al (2006) and Murr and Pizaña (2008), the erosion of a steel target and penetrating KE rod as shown schematically in Figure 4.2.1b and c occurs by solid-state flow of both the eroding projectile and the target, by dynamic recrystallization. This produces a very small (submicron) grain size in both the RET and TET in Figure 4.2.1b and c respectively, which allows them to flow, initially in the same direction toward the entrance surface. This feature is illustrated in the example of a single-crystal [001] oriented W KE rod penetrating a steel target in Figure 4.2.2. In this example, the dynamic recrystallization (DRX) is particularly notable in the projectile because it in fact begins as a single crystal. In the degree of penetration shown in the half-section view of Figure 4.2.2, the RET is observed to be a series of erosion planes flowing one over the other as a result of DRX grain sizes too small to observe. The target TET is also a narrow flow zone, and when the RET flows over the TET, some mixing occurs; even alloying of the Fe target with the W projectile debris tube. Pizaña et al (2006) observed Fe-W or Fe_xW phase regions in the mixing of the RET and TET (Figure 4.2.2) using

energy-dispersive X-ray mapping (or energy-dispersive spectrometry (EDS) mapping) in the scanning electron microscope. Consequently, aerosol particulates (especially nanoparticulates) were observed as speciated Fe (from the target), W (from the projectile) and Fe_xW alloy as a consequence of projectile/target mixing.

In previous work (Machado et al 2010), all debris particulates (D in Figure 4.2.1c) were collected systematically on impacted filters which allowed the size distributions to be controlled, although the large size distributions always contained the complete range of nanoparticulates along with larger particulates.

4.2.2 Particulate Characterization

Selection was taken from a range of commercially manufactured micron and nano-size particles of Fe, W, Ni, and Co from commercial sources in order to emulate possible elemental speciation for WHA rod compositions: 91% (by weight) W, 5.6% Ni, 1.4% Fe; 92% W, 6% Ni, 2% Co. The micron size (powder) particulates were observed directly in a Hitachi S-4800 field-emission scanning electron microscope (FESEM) fitted with an EDAX-EDS system by sticking them to a sampling platform. The nano-size powders were also examined in the FESEM and in a Hitachi H-9500 transmission electron microscope (TEM) operating at 300 kV accelerating potential, employing an EDAX-EDS system. The TEM also employed a digital imaging camera which allowed direct magnifications in excess of 10,000,000 X. The manufactured nanoparticulate powders were sprinkled onto a SiO₂/formvar-coated Cu (200 mesh) TEM grid (3mm diameter) and then sandwiched with another grid on top to contain the powder.

4.2.3 Cell Culture (Viability) Assays

In-vitro cytotoxicity assays were performed for the commercial micron and nano-sized particulates as well on the filter-collected ballistic particulates using a direct contact cell-culture methodology as originally described by Garza et al (2008) and Soto et al (2008). These assays used an

immortalized A549 human epithelial cell line which provides an effective *in-vitro* lung cell model and has been widely adopted as a human lung cell model. The cell line was obtained by the American Tissue Culture Collection (ATCC) from lung carcinomatous tissue from a 58 year old Caucasian male. The A549 cells were cultured in 12-well plates and then exposed for 48hrs (standard time for acute exposures) after the exposure period they were transferred into a 96-well flat bottom plate to assess viability via the MTS Assay. This colorimetric assay assesses relative viability as a function of color, which is directly proportional to the amount of cells available to convert the substrate into a color product. Finally, the absorbance was recorded at 490 nm using a spectrophotometer reader.

4.3 Results and Discussion

4.3.1 Comparison of Manufactured Particulate Microstructures with Reference to Filter-Collected Ballistic Particulates

Figures 4.3.1 and 4.3.2 provide a reference basis for the filter-collected WHA rod – Fe target debris particles for a W-Ni-Fe projectile penetrating a series of 10 Fe target plates 0.63 cm thick and spaced 1.25 cm apart at an initial impact velocity of 1.2 km/s (Figure 1a) (Machado et al 2010). Figure 4.3.1 shows a typical FESEM view of the particulates collected on a filter along with the EDS spectra showing predominantly Fe, with W and C and O. The C peak along with the K, for example, may represent intermixed combustion products, including soot-related nanoparticulates and coatings of other particulates related to the rod propellant composed primarily of nitrocellulose, nitroglycerin, $\text{Ba}(\text{NO}_3)_2$, KHO_3 , ethyl centralite, and graphite. The larger, spherical particulates ($\leq 1.5\mu\text{m}$) are primarily Fe, presumably representing Fe target debris. Note that the smaller range of particulates are aggregated. Correspondingly, Figure 4.3.2 shows a TEM view for the same filter-collected ballistic debris particulates scrapped onto a coated grid sandwich. The nano-size, spherical particulates as in Figure 4.3.1(a) are also generally Fe-rich, while the surrounding, diffuse aggregates are composed of metal or alloy nanoparticles bound by carbonaceous material. There is often a carbonaceous layer surrounding the larger, Fe-rich particulates but this layer often appears to be a complex metal alloy. In addition to

the dominant Fe spectra and notable W, there is a small Ni peak in Figure 4.3.2b but the specific distribution of these elements within the particulates and aggregates is often unclear.

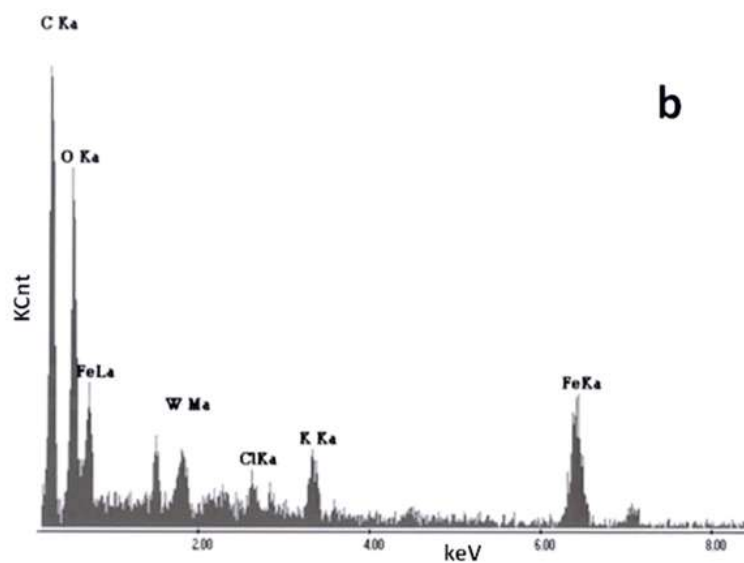
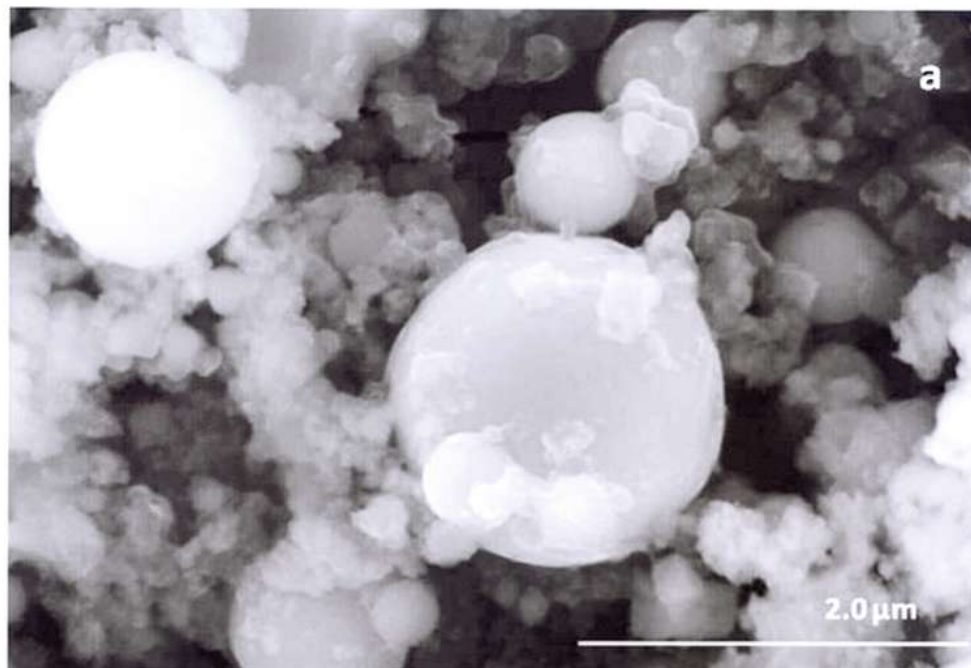


Figure 4.3.1: FESEM view of collected ballistic (impact) debris (a), and the corresponding EDS spectrum (b): W-Ni-Fe.

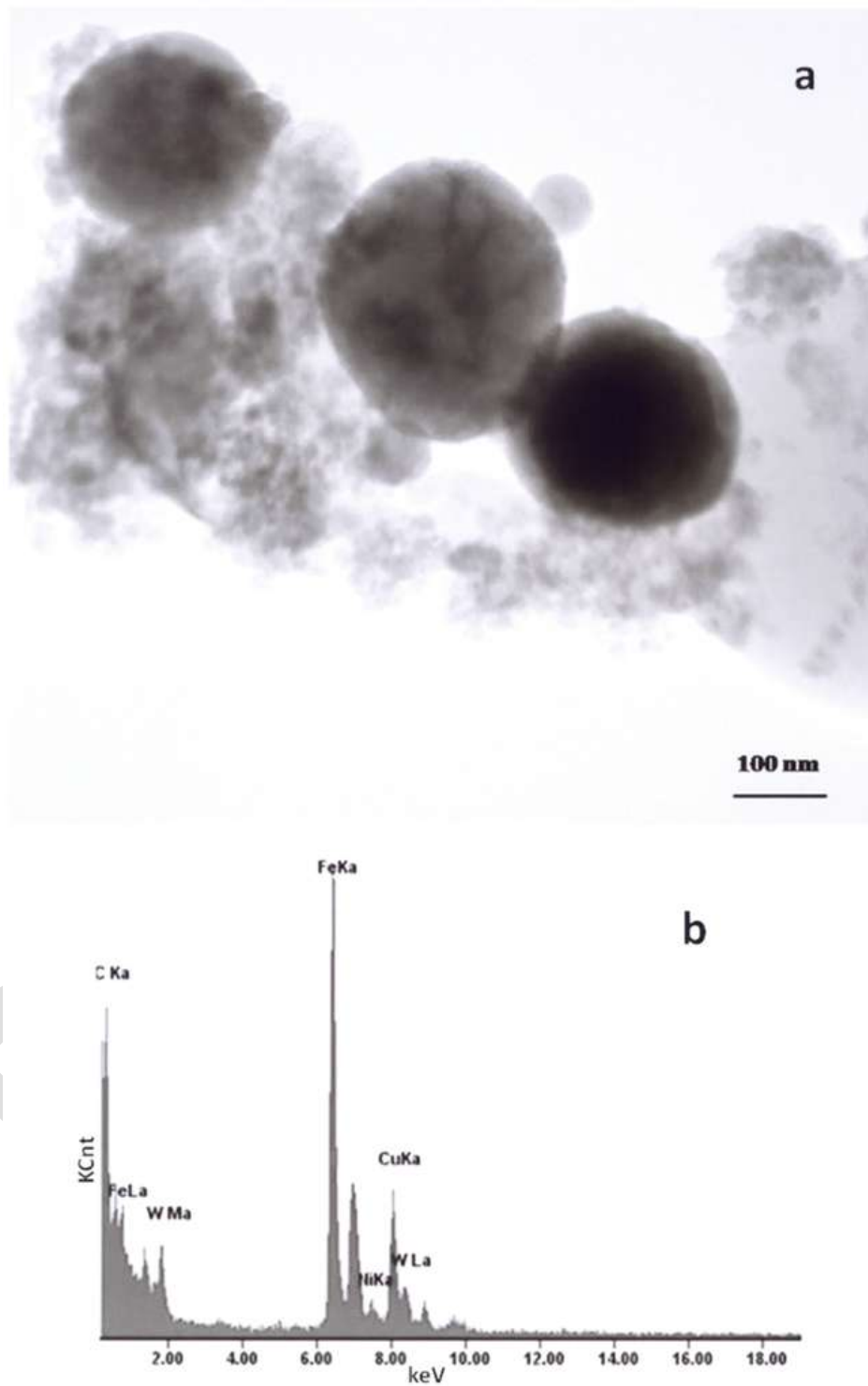


Figure 4.3.2: TEM image of collected impact debris as in Figure 3(a), (a) and corresponding EDS spectrum (b): W-Ni-Fe. Note the sandwich is composed of coated Cu grids. The Cu peak ($K\alpha$) arises from the grid. Note small Ni peak.

Figure 4.3.3 shows a bright-field TEM image and an elemental mapping sequence for W-Ni-Fe ballistic debris similar to Figure 4.3.2, where the larger particles in Figure 4.3.3 are composed of Fe and

some Ni, while the very fine, aggregated nano particle debris is composed primarily of W and Ni. Figure 4.3.4 shows for comparison an elemental mapping sequence for W-Ni-Co ballistic debris also examined in the TEM. The irregular, small nanoparticulate background is observed to be primarily W-rich or nanoparticulate W with more irregular morphologies. There is also some Co associated with the Ni region, which probably represents the ~6% Ni – 2% Co alloy nanoparticulates.

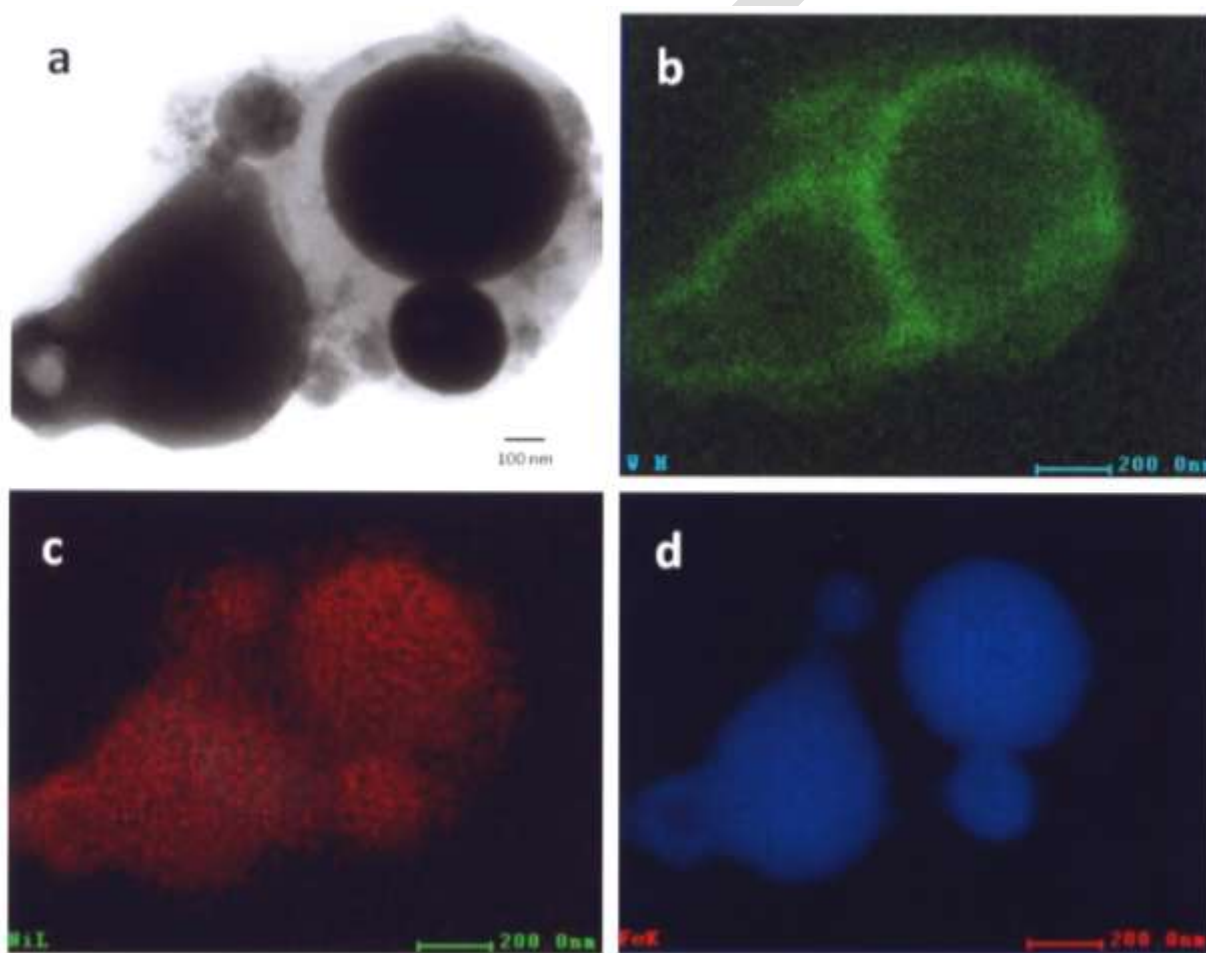


Figure 4.3.3: TEM X-ray (EDS) mapping sequence for W-Ni-Fe ballistic debris sample. (a) Bright-field image of aggregated particulates. (b) W map. (c) Ni map. (d) Fe map.

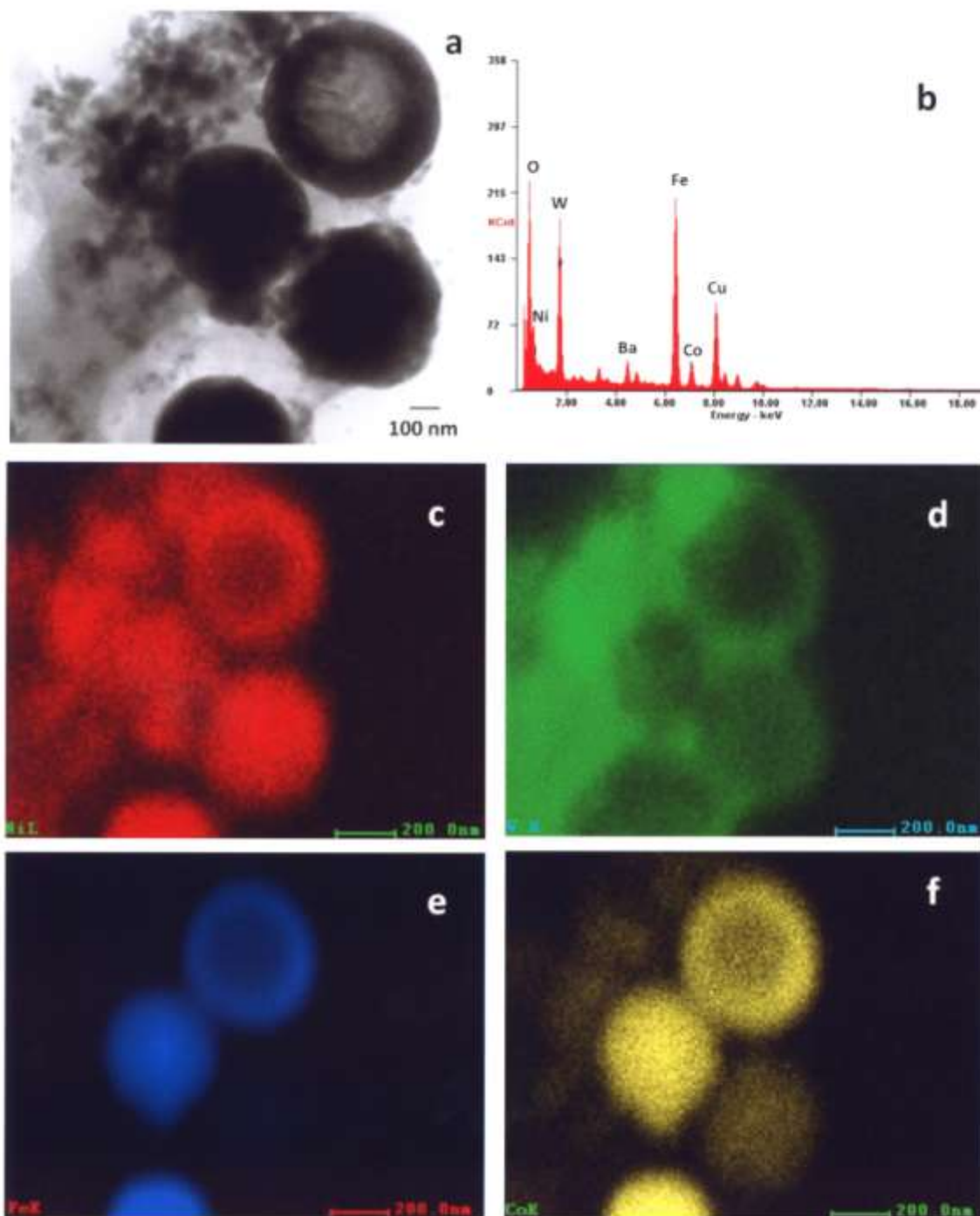


Figure 4.3.4: TEM X-ray (EDS) mapping sequence for W-Ni-Co ballistic debris sample. (a) Bright-field image of aggregated particulates. (b) EDS spectrum of (a). (c) Ni map. (d) W map. (e) Fe (f) Co map.

Figure 4.3.4 illustrates that the larger, spherical or faceted nanoparticles (~ 500 nm) are Ni – Co (with varying ratios of Ni/Co, or Ni-Fe-Co compositions. The upper-right particle in Figure 4.3.4(a) appears to be enclosed by a ring-like zone composed of Ni-Fe-Co with a lower concentration of W.

Consequently, the larger, spherical micron-size particulates as shown in the FESEM view of Figure 4.3.1(a) appear to be Fe or Fe-rich, while the nano-size spherical particulates in the TEM views in Figure 6 are alloy mixtures of Fe-Ni-Co or Ni-Fe. The smallest, aggregated nanoparticulate regimes are irregular, elemental W (≤ 50 nm), along with some Ni-Co or Ni-Fe alloy nanoparticulates representing the projectile matrices, respectively; although some of this aggregated nanoparticulate debris may be Ni-rich. The metal-rich ring surrounding a spherical particle in Figure 4.3.4a may also represent matter created by metal or alloy vapor in the same way that some metal particulates, particularly Fe, appear to be coated with carbonaceous matter (Machado et al. 2010). The lower right elemental map shows Ni, Fe, and very strong Co in the spherical-like particles while the W is, as noted, prominent in the nano-debris area to the left, along with Ni as shown in the first elemental map for Ni.

In comparison to the ballistic debris collections examined in Figures 4.3.1 to 4.3.4, the manufactured particulate powders exhibited similar morphologies. These are illustrated typically in the sequence of FESEM and TEM observations shown in Figures 4.3.5 to 4.3.13. Figures 4.3.5 and 4.3.6 show two varieties of micron-size Fe and W, at different magnifications. The Fe particulates in Figure 4.3.5a and c are recognizably aggregated in the manufacturing process. The Fe particles are generally spherical while the W particles are notably faceted single crystals.

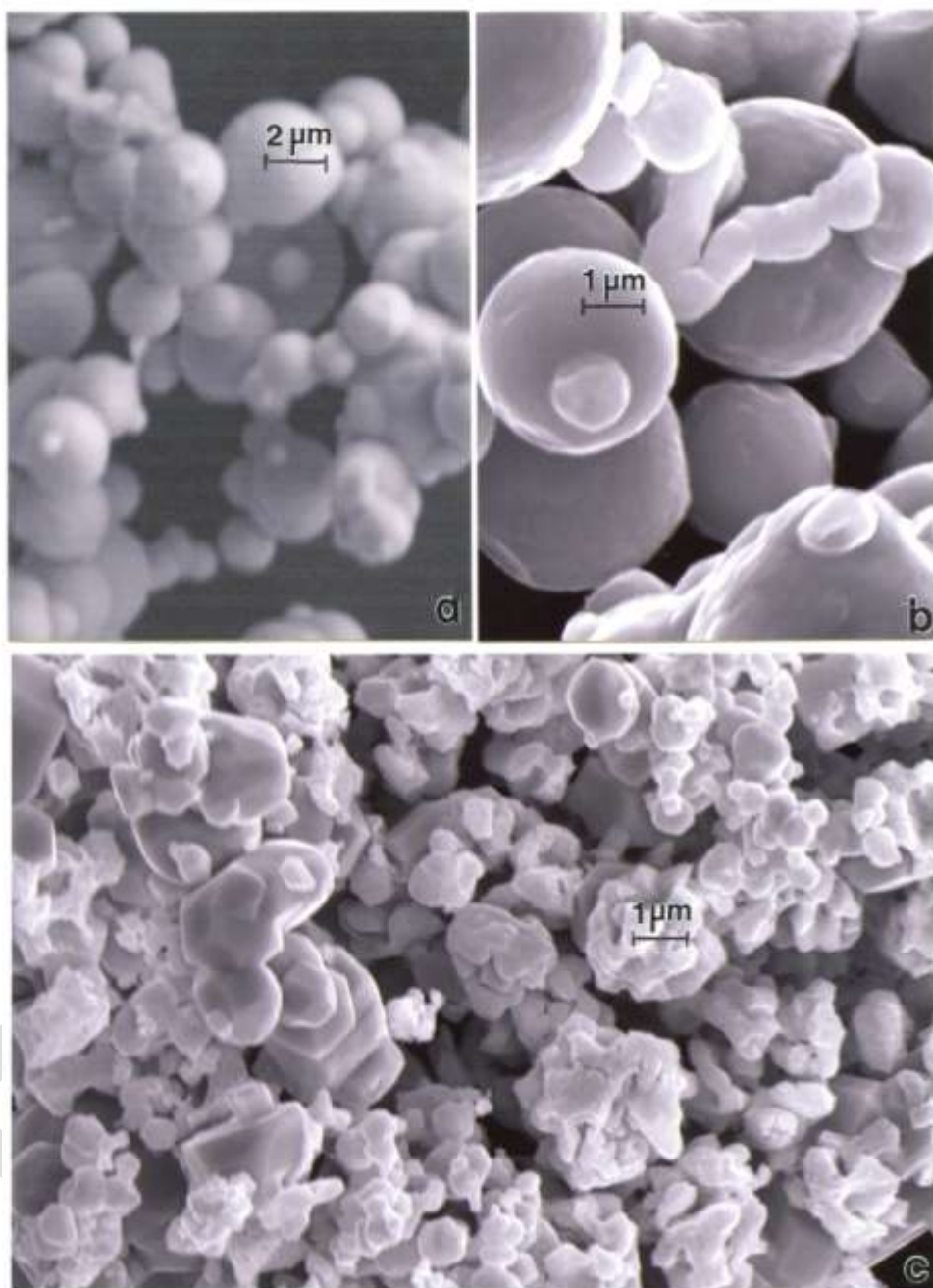


Figure 4.3.5: FESEM images of Fe and W micron-size powders. (a) Fe (ESPI, Inc.). (b) Fe (Aldrich). (c) W (Buffalo Tungsten, Inc.).

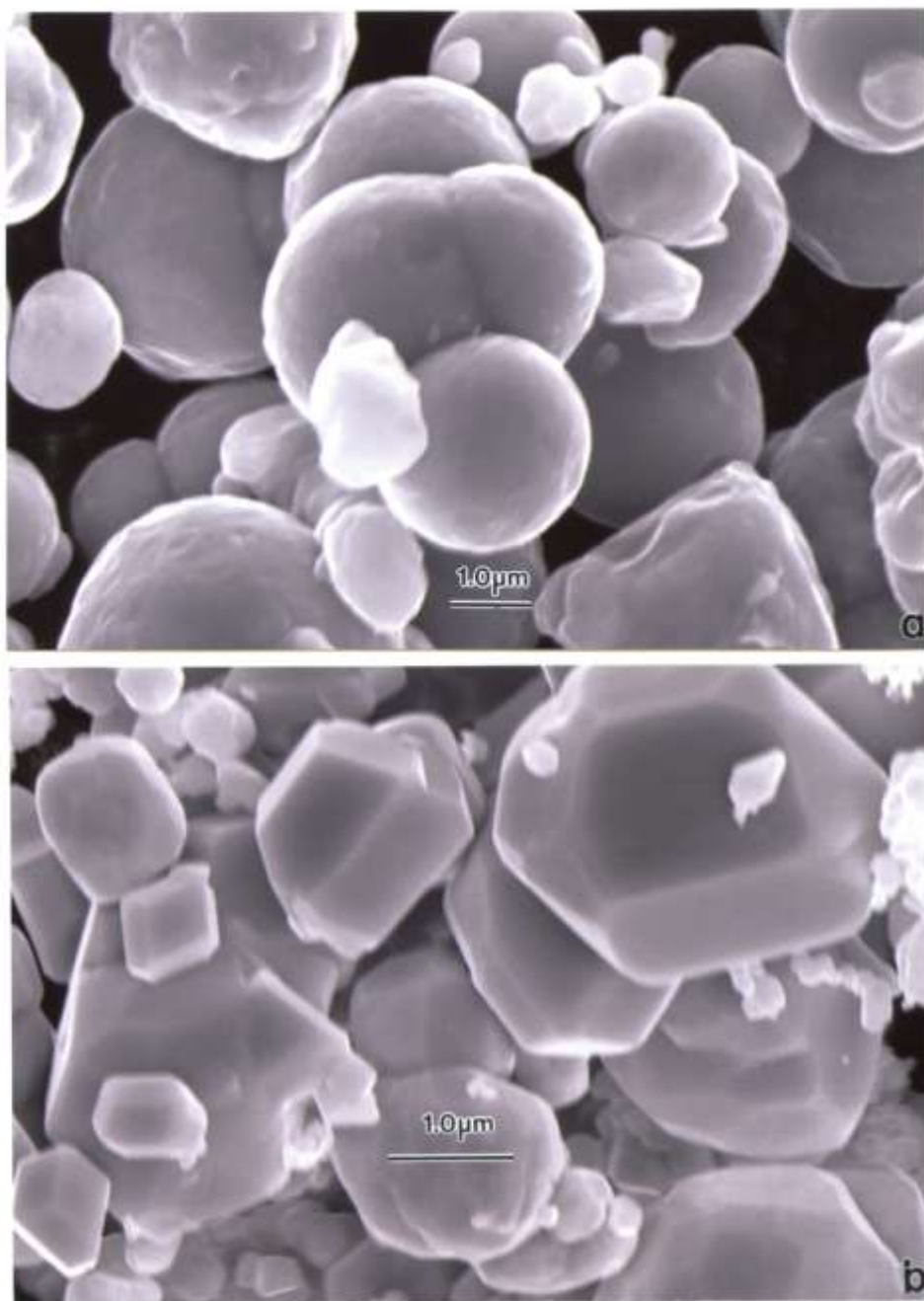


Figure 4.3.6: Magnified FESEM images for Fe and W micron-size powders. (a) Fe (Aldrich). (b) W.

Figures 4.3.7 and 4.3.8 compare nanoparticulate Fe and W powders, respectively in the TEM, while each image also contains an FESEM insert. These particulates are also aggregated but contain a high fraction of very small particulates (5-50 nm) in contrast to a larger range of μm size, spherical

particles, creating a broad, nano-size distribution with a smaller distribution of micron-size particles (1-3 μm diameter); creating a skewed, bimodal size distribution toward the small nanoparticulate range.

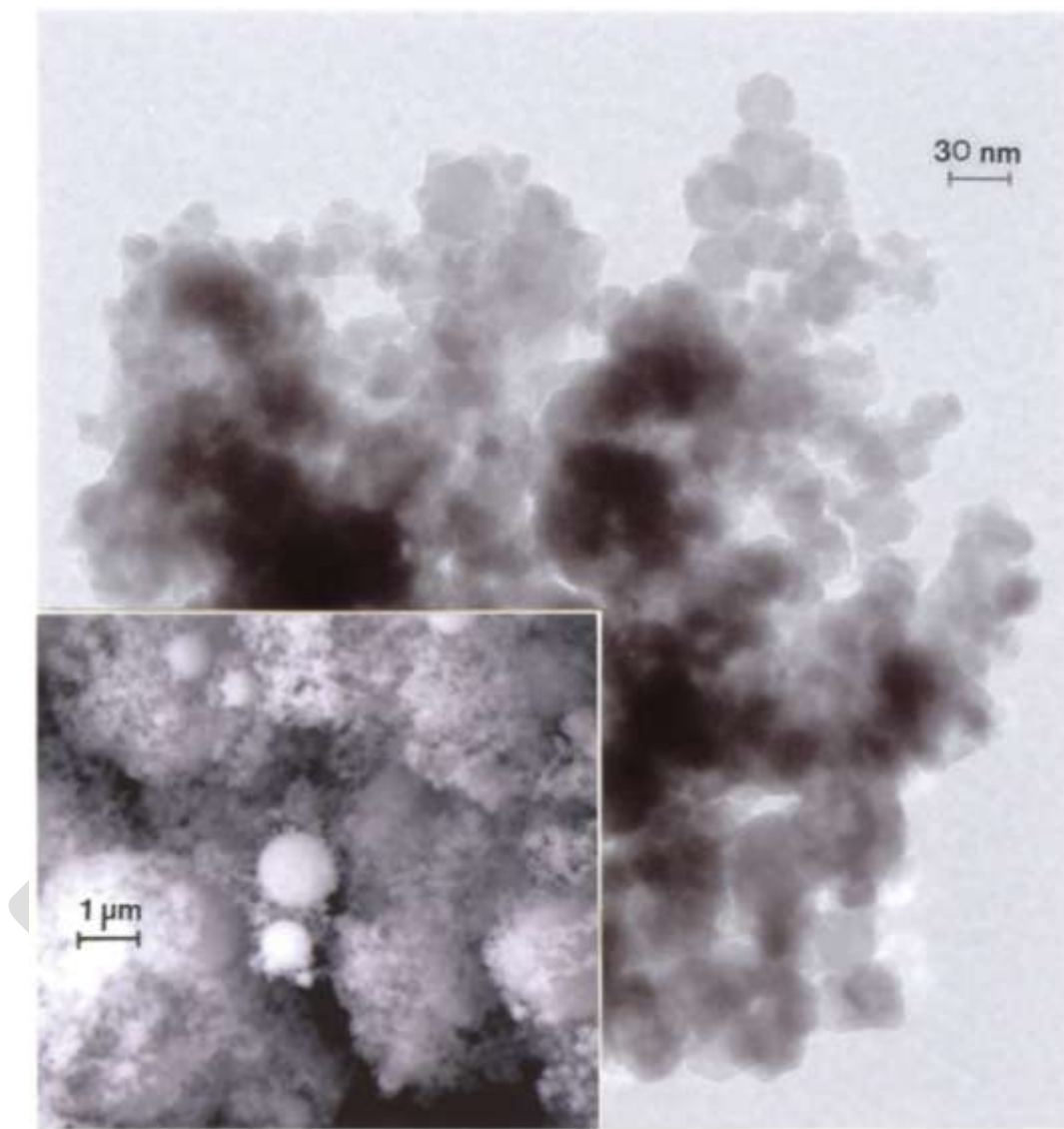


Figure 4.3.7: TEM image for nano-Fe powder with FESEM image insert showing nanoparticulate aggregation.

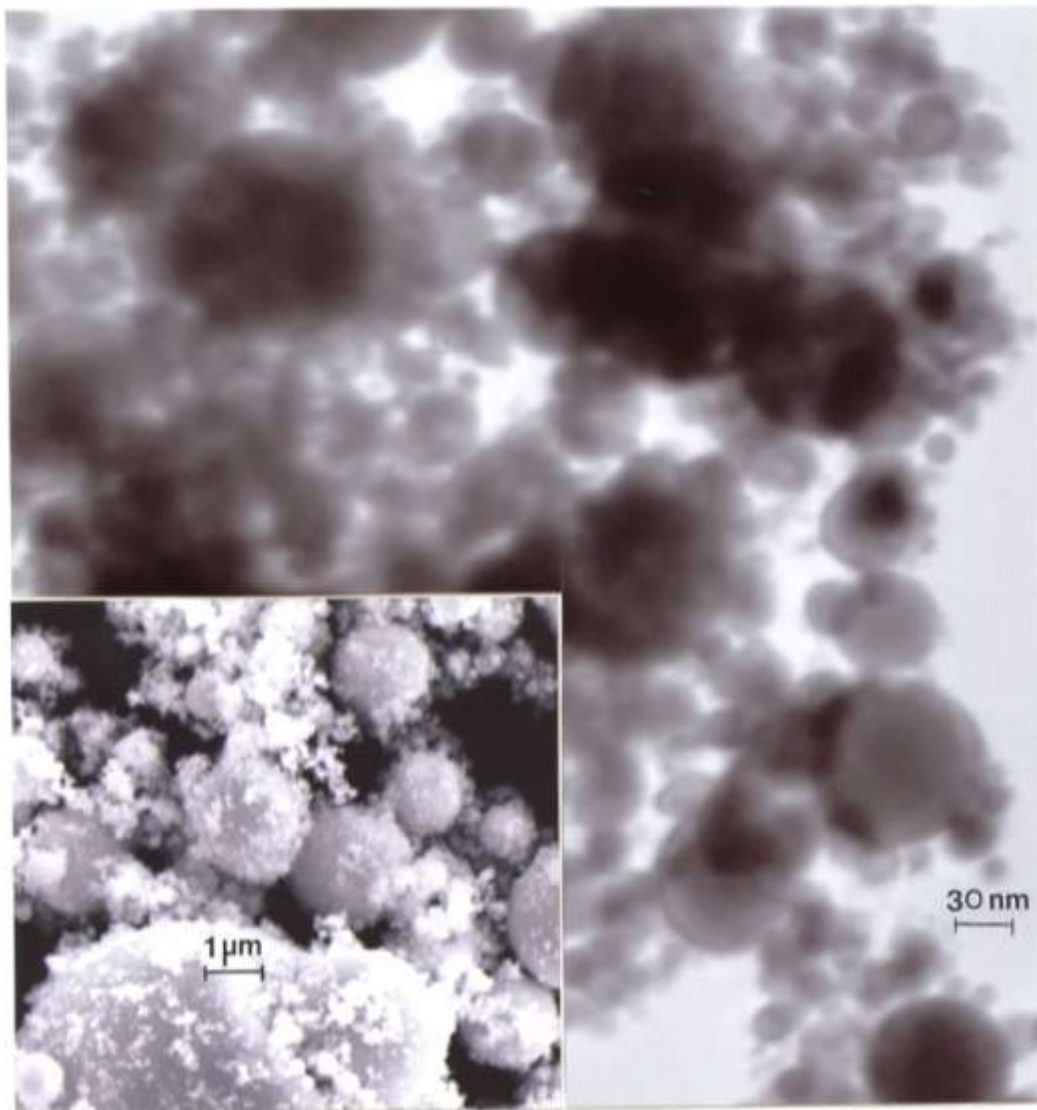


Figure 4.3.8: TEM image for nano-W powder with FESEM image insert showing nanoparticulate aggregation.

Figure 4.3.9 compares the micron or near-micron-size powders for Ni and Co, respectively. In contrast to the micron-size Fe and W powders in Figures 4.3.5 and 4.3.6, the generally aggregated Ni and Co powders are generally less than or equal to $\sim 1\ \mu\text{m}$, in contrast to the Fe and W powder particle sizes which include particle sizes $\leq 3\ \mu\text{m}$. Nonetheless, these particulates exhibit a very narrow size distribution averaging roughly $0.8\ \mu\text{m}$.

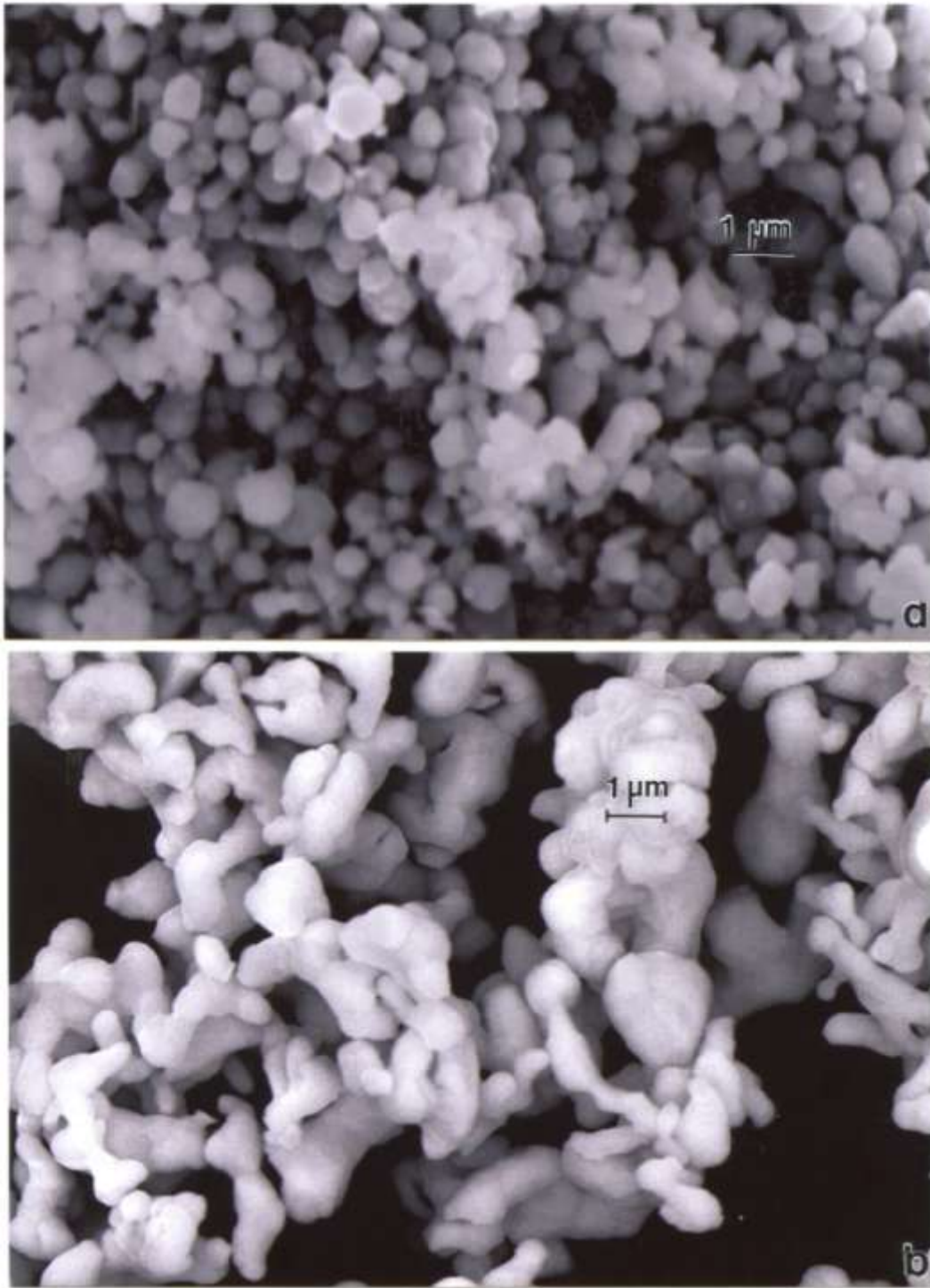


Figure 4.3.9: FESEM images for Ni (a) and Co (b) micron-size powders.

Figures 4.3.10 to 4.3.11 compare the nano-size Ni and Co powders. The aggregated Ni particulates in Figure 4.3.10 exhibit growth twins in otherwise perfect single crystal particles. The FESEM insert in Figure 4.3.10 shows the aggregated, dominant nano-particle size distribution. Figure

4.3.11 compares the nanoparticulate Ni in bright-field and dark-field (Figure 4.3.11a and b) imaging utilizing a small portion of the fcc selected-area electron diffraction pattern insert. The dark-field image confirms the single-crystal particulate nature and also illustrates their size and morphology more definitively. Correspondingly, Figure 4.3.12 shows a TEM image for the Co nanoparticulates with an FESEM image insert. These nanoparticulates are also aggregated in a fashion similar to the micron-size particulates shown in Figure 4.3.9b.

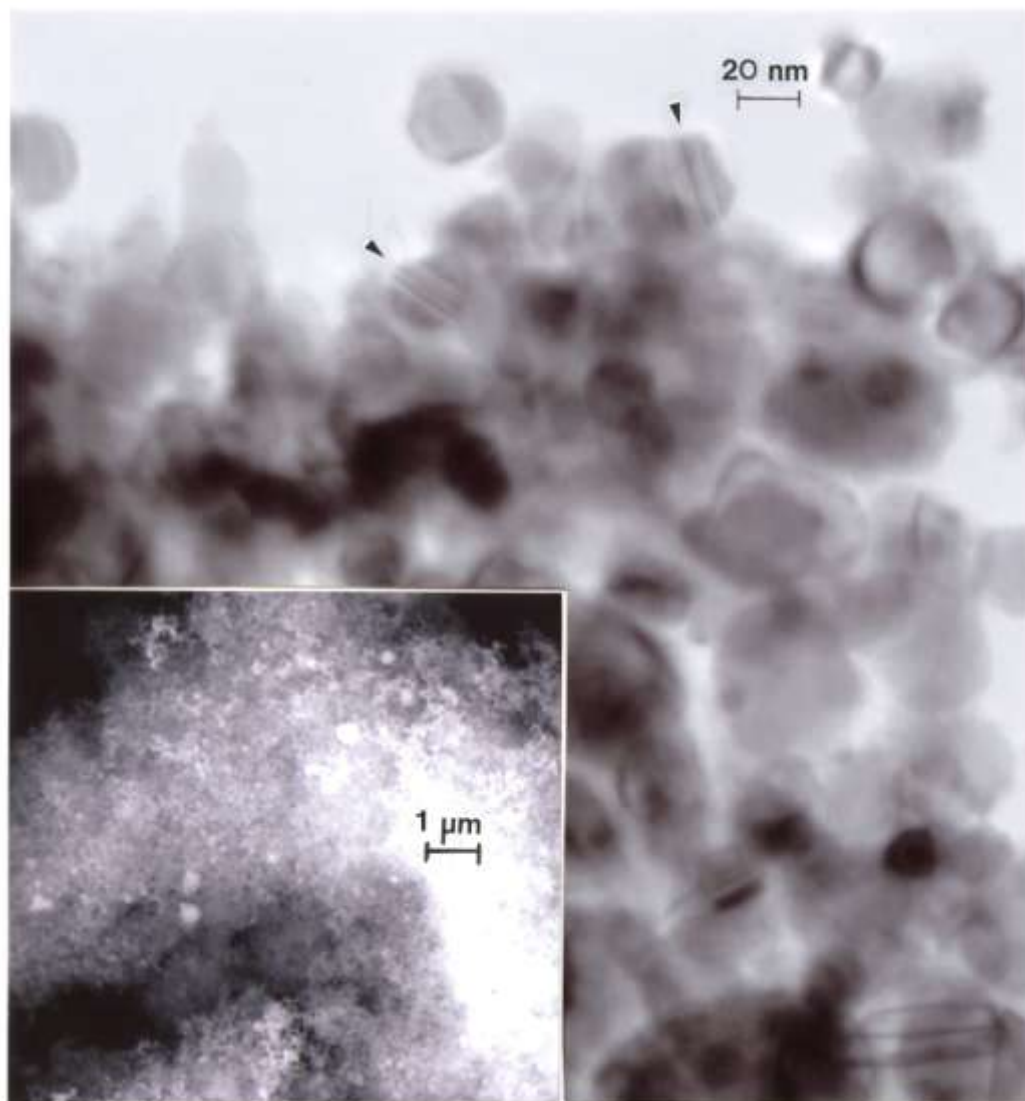


Figure 4.3.10: TEM image for nano-Ni powder with FESEM insert showing nanoparticulate aggregation. The features noted by arrows are microstructural twins in the particles.

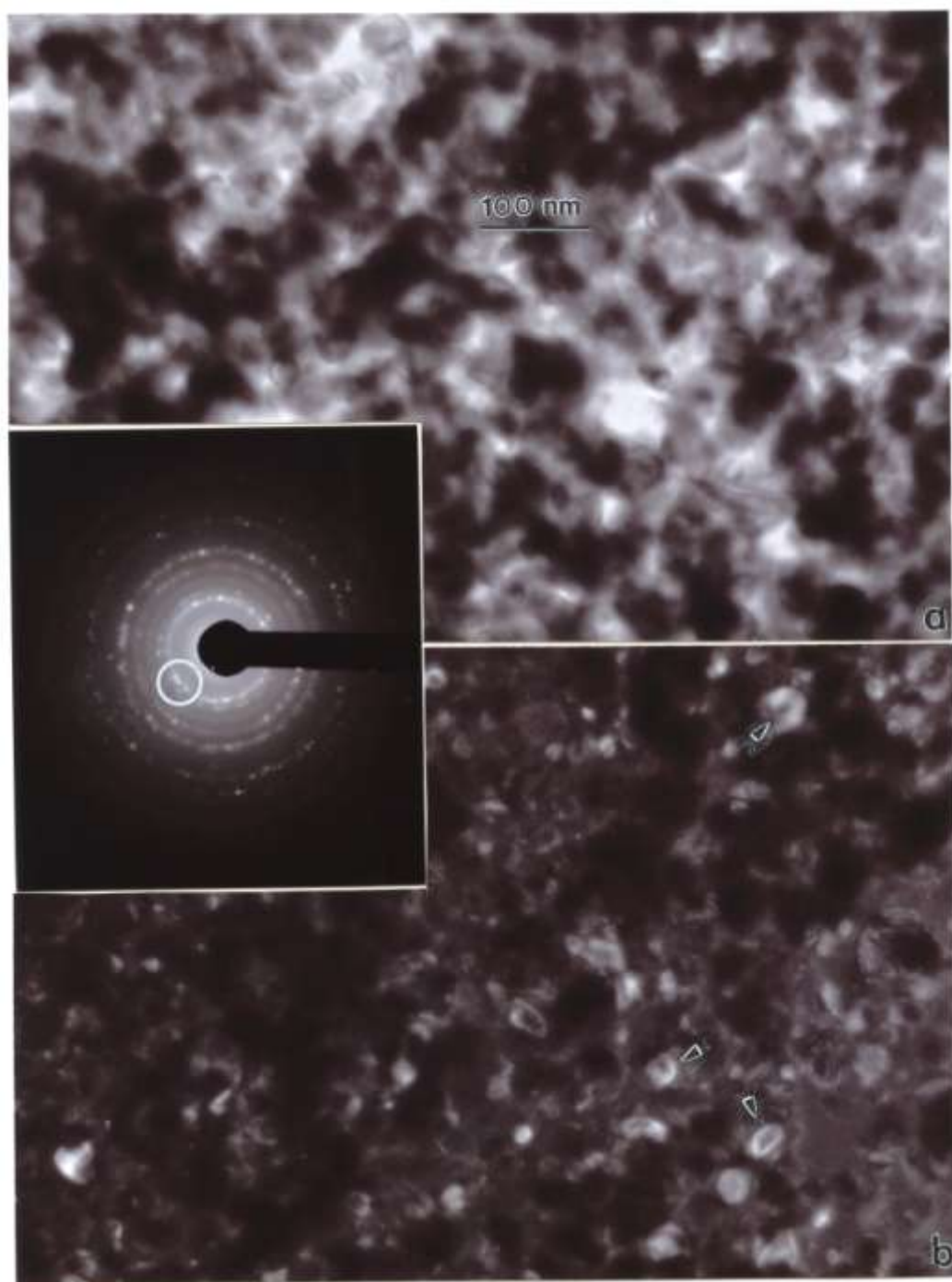


Figure 4.3.11: TEM bright-field (a) and dark-field (b) sequence for nano-Ni powder utilizing selected diffraction spots from the selected-area electron diffraction pattern insert (circle). Arrows in (b) show diffracting nanoparticles.

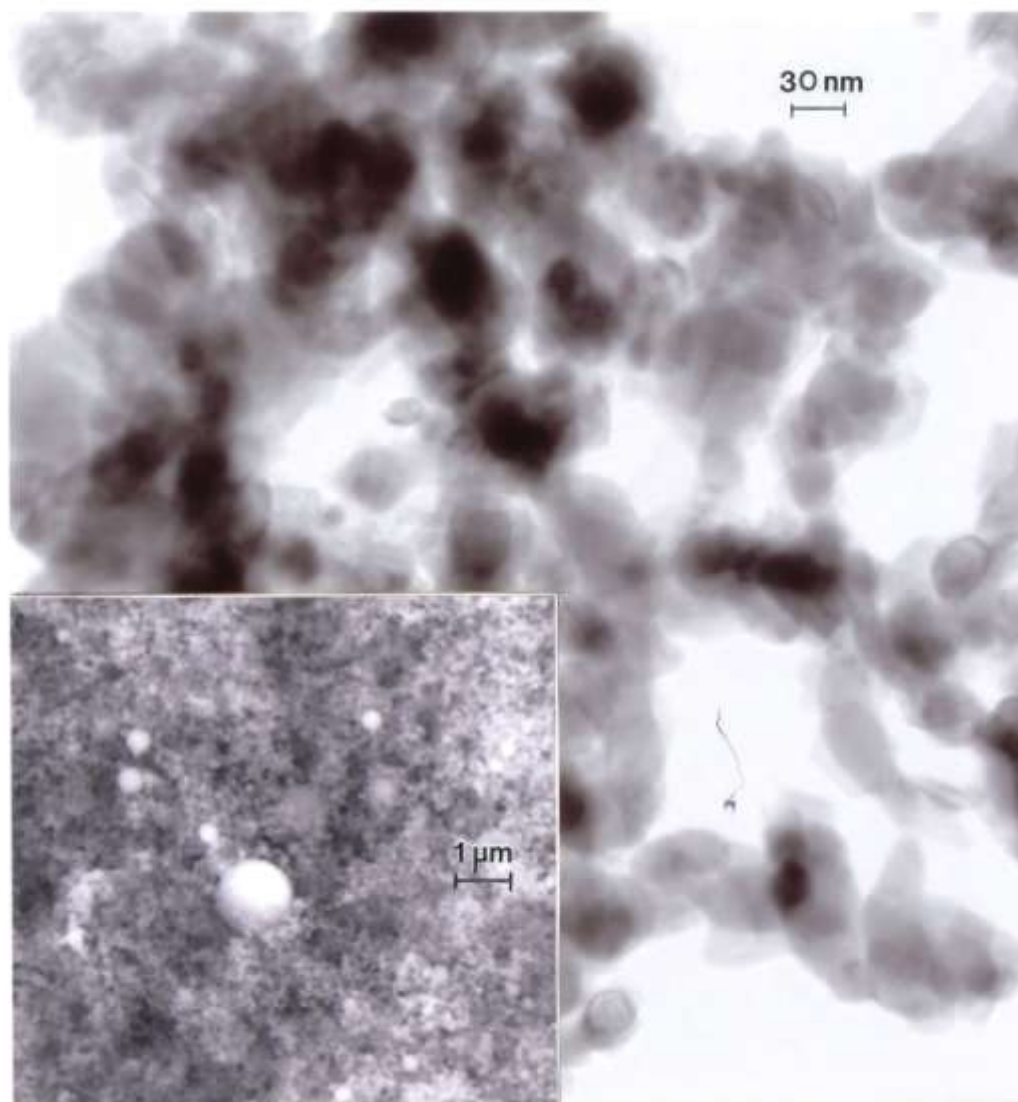


Figure 4.3.12: TEM image for nano-Co powder with FESEM insert showing nanoparticulate aggregation.

Figure 4.3.13 shows a high-resolution TEM image for an aggregate of Co nanoparticulates which confirms the single-crystal, sintered particle nature. There is also evidence for an oxide layer enclosing the particles, while the Moire fringe pattern illustrates the extent of the Co crystal structure within an amorphous oxide layer ~3 nm thick.

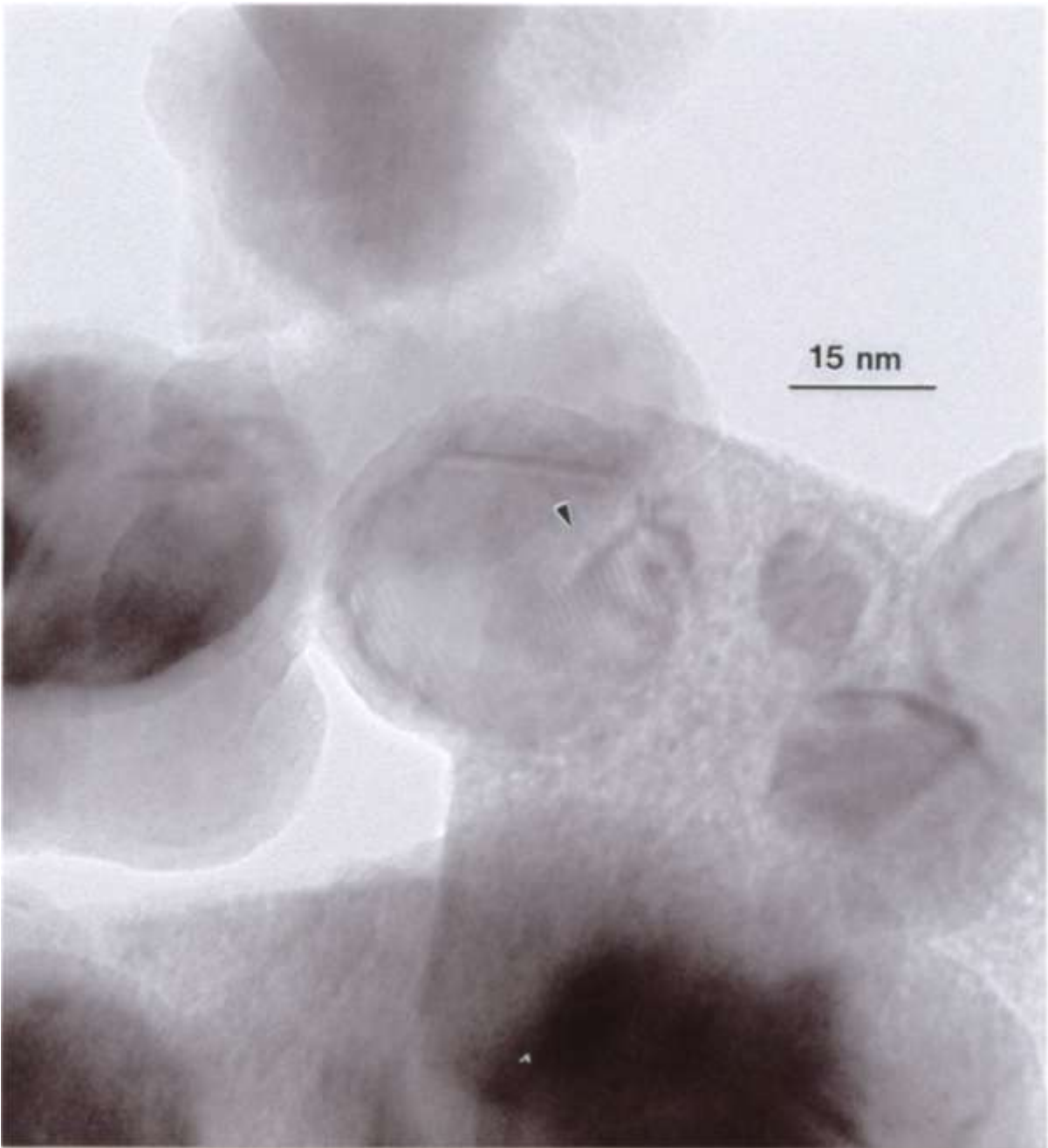


Figure 4.3.14: High resolution TEM image for nano-Co powder aggregates showing Moire fringe pattern with 1.3 nm fringe spacing (arrow).

Particle size distributions were measured for the manufactured micron-range size and nano-range size powders illustrated comparatively in Figures 4.3.5 to 4.3.13, and noted the size range or width of the size distribution. In addition we measured the average size for each size-range of particles. These measurements along with other particle properties are listed in Table 4.3.1.

Table 4.3.1: Experimental (Manufactured) Powder PropertiesMicron-Range

Element	Size Range (μm)	Ave. Size (μm)	Crystal structure	Lattice Parameter (nm)	Particle Morphology
Fe ¹	0.4-4	3	bcc	0.29	Spherical
Fe ²	1-6	3	bcc	0.29	Spherical
Ni	0.2-1	0.6	fcc	0.35	Spherical
W	0.2-3	1	bcc	0.32	Faceted
Co	0.3-2	1	fcc	0.35	Spherical

Nano-Range

Element	Size Range (nm)	Ave. Size (nm)	Crystal structure	Lattice parameter (nm)	Particle Morphology
Fe	10-2000	30	bcc	0.29	Spherical
Ni	10-500	27	fcc	0.35	Spherical
W	6-5000	37	bcc	0.32	Spherical
Co	10-1000	33	fcc	035	Spherical

Notes: 1. ESPI, Inc. (supplier); 2. Sigma-Aldrich S.A. (supplier)

4.3.2 Viability Assays and Assay Comparisons

In-vitro assays in A549 human epithelial cell cultures for 48h for several assay groups representing ballistic debris collections reproduced from prior work by Machado et al (2010) are shown in Figure 4.3.14a and b. These assays demonstrate that the A549 cells were killed so extensively that only aggregates of the nanoparticulates uptaken by the cells remained, particularly for sample 11 and 3.

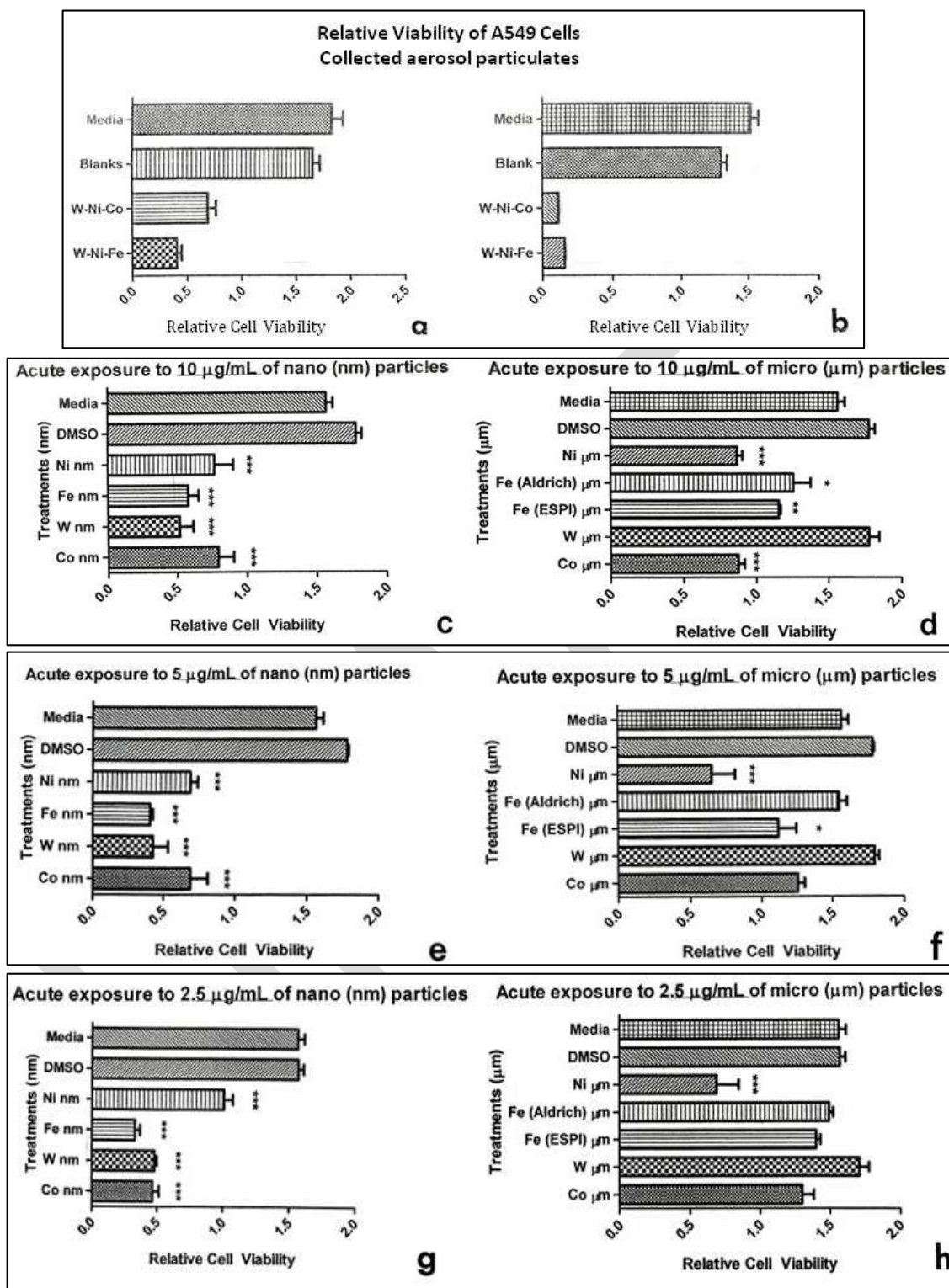


Figure 4.3.14: Comparative cytotoxicities (as relative A549 epithelial cell viability). (a) and (b) show collections for 4 separate ballistic events: 2 for W-Ni-Fe and 2 for W-Ni-Co KE rods penetrating Fe target plates. (c) and (d) compare nano and micron-size powders at concentrations in culture of 10 µg/mL. (e) and (f) compare nano and micron-size powders at concentrations in culture of 5 µg/mL. (g) and (h) compare nano and micron-size powders at concentrations of 2.5 µg/mL. All cell culture assays ((a) to (h)) are compared to culture media as a control. (a) and (b) also show blank filter culture as a control. (c) to (h) show DMSO as a control. Key note: $p<0.05$ = *, $p<0.0015$ = **, $p<0.0001$ = ***.

Figure 4.3.14c, e, and g show, in comparison with Figure 4.3.14a and b, that the single component (elemental) metal nanoparticulates (Table 4.3.1) exhibit notable cytotoxicity, but not as significant as the mixture of ballistic debris particulates shown in Figure 4.3.14a and b, especially for low concentrations in culture as shown in Figure 4.3.14g. There is a slight dominance of cytotoxic response for Fe and W nanoparticulates (Table 4.3.1), but not statistically significant. In contrast, Figure 4.3.14d, f, and h show that for varying concentrations of micron-size metal particulates in culture, there is no notable cytotoxicity as measured by cell viability; although the consistent (if insignificant) slight decline in viability for Ni may reflect the fact that it is at the upper nanometer size range, and the smallest size micron powder (Table 4.3.1).

Inhaled particulates (including coarse nanoparticles $<1\ \mu\text{m}$) initially encounter the mucociliary clearance by cilia of the bronchial epithelial cells which moves the larger particles ($>1\ \mu\text{m}$) towards the upper respiratory tract. However the truly nanoparticles ($<1\ \mu\text{m}$) migrate to the alveoli where phagocytes and other cells with phagocytic abilities work to arrest them. However with phagocytic impairment, or for nanoparticles $<100\ \text{nm}$ which are not readily phagocitized, nanoparticles can accumulate and even aggregate to create oxidative stress and inflammation (Oberdörser et al 1994). This can lead to various diseases while inflammation plays a major role in coronary heart disease and airway diseases such as asthma and chronic obstructive pulmonary disease (COPD). A prominent mechanism responsible for the variety of nanoparticle toxicities assumes a shift in the redox balance of the cells towards oxidation as a consequence of the formation of reactive oxygen species (ROS) which can, in the longer term, lead to DNA damage (Buzea et al 2007). In addition to oxidative stress, some nanoparticles can enhance the expression of specific viral receptors and lead to severe inflammation when exposed to viral infections while other nanoparticles can decrease the expression of certain viral and bacterial receptors which lowers the resistance to some types of micro-organisms (Dobravolkala et al 2007).

While the *in-vitro* cell culture results for varying concentrations of elemental metal nanoparticulates (Fe, W, Ni, Co) shown in Figure 4.3.14c, e and g are not as significant as those in Figure 4.3.14b, the lowest concentration in culture (Figure 4.3.14g) is comparable with Figure 4.3.14a, except for the Ni. Figure 4.3.14c-h illustrate that, consistent with many prior studies (Donaldson et al. 2001; Oberdörser 2001; Pope and Dockery 2006) there is measurable, and measurably greater cytotoxic, *in-vitro*, response for the nano-metal powders in contrast to the micron-size powders; although Oberdörser et al (1994) have concluded that aggregated nanoparticles are not as toxic as smaller concentrations of single particles. Nonetheless, since essentially the entire ballistic aerosol regime as well as the elemental nanoparticles are aggregated (Figures 4.3.1-4.3.13), this finding does not detract from the demonstrated cytotoxicity in Figure 4.3.14. In addition, Murr et al (2008) have shown that a wide range of aggregated nanoparticulate species are noticeably cytotoxic, including a wide range of metal oxides and nano-soots.

In order to investigate the potential cytotoxic synergism of the rod alloys or mixtures of nano particle elements, cell culture studies identical to those shown in Figure 4.3.14 were conducted for mixtures of both the micron-size powders and the nano-powders: (Fe + W), (Fe + Co), (Fe + Ni); in 50/50 mixtures in culture at concentrations of 10 µg/mL, 5 µg/mL, and 2.5 µg/mL (data not shown). The micron-size powder particle mixtures showed no cytotoxic response, consistent with the single-component powders in Figure 4.3.14d, f, and h. There was a small but statistically insignificant cell viability reduction for the (Fe + Co) nanoparticulate mixture, leading to the conclusion that elemental nanoparticulate synergism is apparently not an important contributor to the cytotoxic behavior observed for the ballistic aerosol in Figure 4.3.14a and b.

Figures 4.3.3 and 4.3.4 have already demonstrated the propensity for W and Ni nanoparticulate aggregates especially elemental nanoparticulates in the range of 5 to 10 nm; with some elemental mixing especially in larger nanoparticles, possibly as a result of projectile erosion and mixing with the Fe target

erosion regime by dynamic recrystallization as illustrated in Figure 4.2.2. On considering Figures 4.3.3 and 4.3.4 in comparison with the results of Figure 4.3.14a and b, and Figure 4.3.14c, e, and g with Figure 4.3.14d, f and h, there seems to be compelling evidence for significant cytotoxic response for W, Fe, Ni and Co nanoparticulates in contrast to micron-size particulates of these elements. Consequently, on perusing Figures 4.3.2-4.3.4 retrospectively, it would appear that the ballistic debris cytotoxicity shown in Figure 4.3.14a and b results by the smallest nanoparticulate aggregates of W, or possibly Ni-Co or Ni-rich nanoparticles < 10 nm. This conclusion also points to the prospect that it is primarily the WHA projectile which exhibits or induces the significant cytotoxicity for ballistic, aerosol debris.

4.4 Conclusions

Ballistic aerosol as well as manufactured micron and nano-sized particles representing the ballistic alloy compositions: W, Fe, Ni, Co, were characterized and exposed to cytotoxic experiments using a human epithelial A549 (lung model) cell line. Earlier work by Machado et al (2010) has shown that the ballistic aerosol collections of aggregated nanoparticles averaging ~10 nm, were highly toxic to this cell type in a very short time (48 h), i.e., the cells were killed so rapidly that there was no time to produce any anti-inflammatory markers, Interleukin 6 and 8 (IL-6 or IL-8). They are anti-inflammatory cytokines that stimulate immune response to trauma that leads to inflammation, such as tissue damage. Nanoparticles of Fe/W; W/Ni; W/Co, etc. exhibit noticeable cytotoxicity but not as significant as the mixture of ballistic aerosol. Although the commercially manufactured nano and micron particles do not contribute significantly to epithelial cell death, there is a measurably greater cytotoxicity for the nano powder particulates in contrast to the micron-size particulates, in agreement with many other comparative studies (Murr et al, 2008; Oberdörster, 2001; Pope and Dockery, 2006). The characterization of the ballistic aerosol particles in comparison to the commercial (manufactured) powders shows similar morphologies for both the nano and micron size using SEM and TEM analyses. EDS elemental mapping sequences of the collected ballistic aerosols show that the larger (micron)

particles are mainly Fe, but reveal mixtures, of primarily W and Ni composing surrounding nano-size, aggregated particles. There are limited observations regarding small particles and aerosols, chemistries, size distributions and cytotoxic responses for this type of alloys and elements. Likewise, studies performed in other particles with a vast compositional range and microstructural characteristics exhibit respiratory inflammatory effects.

Taken together, the results of cytotoxicity assays indicate potential respiratory effects for manufactured elemental (W, Ni, Fe, Co) nanoparticles, especially W and Fe while the collected ballistic aerosols, either W-Ni-Co or W-Ni-Fe exhibit extreme cytotoxicity, and potential for serious health effects, especially short-term. While W is normally not toxic in bulk or micron-size form, nano-W exhibits measurable cytotoxicity.

4.5 Acknowledgements

This research was supported in part by the U.S. Army Research Laboratory (ARL), Aberdeen Proving Ground, MD (under Contract No. W9119X-08-D0001, Amend. #0002); the NIH-funded RCMI Grant #2G12RR008124. A Mr. and Mrs. MacIntosh Murchison at the University of Texas at El Paso also provided partial support. R.M.S. is supported by a RISE Graduate Student Fellowship Grant #R25GM069621-02. The two cores used for the cell analyses were the following: (a) Cell Culture and High Throughput Screening (HTS) Core Facility and (b) The Biomolecule Analysis Core Facility.

4.6 References

- Buzea, C., Pacheco, J, Robbie, K. 2007. Nanomaterials and nanoparticles: sources and toxicity. *Biointerphases*, 2: 17-71.
- Dobravolvkala, M.A., McNeil, S.E. 2007. Immunological properties of engineered nanomaterials. *Nature Nanotechnology*, 2: 469-478.
- Donaldson K., Stone V., Clouter A., et al. 2001. Ultrafine particles. *Occup Environ Med*, 58: 211-15.

- Garza, K.M., Soto, K.F., Murr, L.E., 2008. Cytotoxicity and reactive oxygen species generation from aggregated carbon and carbonaceous nanoparticulate materials. *Int J Nanomed*, 3(1): 83-94.
- Gold K., Cheng T.D., Holmes A., 2007. A quantitative analysis of aerosols inside an armored vehicle perforated by a kinetic energy penetrator containing tungsten, nickel and cobalt. *Military Med*, 172 (4): 393-98.
- Guilmette, R.A., et al. 2006. Human health risk assessment of capstone depleted uranium aerosols. Attachment 3 of depleted uranium aerosol doses and risk: Summary of U.S. Assessments, Battelle Press, Columbus, OH.
- Machado, B.I., et al. 2010. Characterization and cytotoxic assessment of ballistic aerosol particulates for tungsten alloy penetrators into steel target plates. *Int J Environ Res and Public Health*, in press.
- Murr, L.E., Pizaña, C. 2008. DRX: The dynamic deformation regime. *Metall Mater Trans A*.
- Murr L.E., Soto K.F., Garza K.M., 2008. Health hazards of manufactured, natural environmental and anthropogenic atmospheric nanoparticulate materials: Past, present and future. In Chapter 1 *Biomaterial and Biomedical Engineering*, ed. A. Oechsner A, 1-54. trans. Tech Publishers: Switzerland.
- Oberdörser, G., Ferin, J., Lehnert, B.E. 1994. Correlation between particle size, in vivo particle persistence, and lung injury. *Environ Health Perspect*, 102: 173-179.
- Oberdörser, G., 2001. Pulmonary effects of inhaled ultrafine particles. *Int. Arch. Occupat. Environ. Health*, 74: 1-8.
- Pizaña, C., et al. 2006. Solid-state flow, mechanical alloying, and melt-related phenomena for [001] single-crystal W ballistic rod penetrators interacting with steel targets. *Mater. Sci. Eng A*, 428: 301-13.

Pope III, C.A., Dockery, D.W., 2006. Health effects of fine particulate pollution: Lines that connect. *J. Air and Waste Manage Assoc*, 56: 709-42.

Soto, K.F., et al. 2008. Direct contact cytotoxicity assays for filter-collected, carbonaceous (dust) nanoparticulate. Material and observations of lung cell response. *Atmos Environ*, 42: 1970-82.

DRAFT

Chapter 5: Materials Characterization of Railgun Erosion Phenomena

The material of this chapter has been accepted for publication with minor revisions in the Materials Science and Engineering A Journal under manuscript ID # MSA_MSEA-D-11-01178

Abstract

This paper describes the observations of aluminum projectile (or armature) tribomaterial deposition onto copper (stator) conducting rails in an experimental solid-armature railgun system, by optical, and scanning and transmission electron microscopy. The extreme deformation at the aluminum/copper interface creates a solid-state flow regime by dynamic recrystallization which also leads to the erosion-product deposition. Melting of the low-temperature aluminum deposit also contributes to the rail damage and degradation of electromagnetic behavior. The creation of nano-grains by dynamic recrystallization allows for mixing at the aluminum/copper interface, and there is no evidence for traditional alloying.

5 Materials Characterization of Railgun Erosion Phenomena

B.I. Machado, L. E. Murr, E. Martinez, S. M. Gaytan and S. Satapathy

5.1 Introduction

The development of single, pulsed homopolar generator – inductor railgun systems has been ongoing for more than four decades (Chiltron et al 1977; Marshall 1994; and Meger 2005). The simplest design configuration involves an electrically pulsed-power gun or electromagnetic launcher, that accelerates a conductive projectile along a pair of conducting metal rails using the same principles as the homopolar motor; with the projectile acting as an armature making contact with the rails. The conventional railgun design is shown schematically in Fig. 5.1.1 and more conceptually in Fig. 5.1.2 as applicable to this study. As illustrated in Fig. 5.1.1, a very high current (I) is passed through the rails and the solid armature (projectile). This projectile current interacts with the strong magnetic fields generated by the rails, and this interaction produces a strong (pulsed) force, the Lorentz force (F), where $F = (\mu_o I^2)/(ln(d-r)/r))/\pi$ with reference to Fig. 5.1.1, and μ_o is the magnetic permeability of free space. This accelerates the projectile to hypersonic velocities (≥ 2 km/s; Mach 10) for multi-kilogram masses. Energies as high as 10 MJ (and $I \sim 1$ MA) from capacitor bank storage have been recently tested (Peterson 2008) with prospects of launching projectiles 200 nautical miles at energies of 64 MJ. The utility of railguns involves their range and velocity, which are commensurate with short-range missiles but at considerably lower cost. In addition there is no explosive hazard, no shell extraction, and the prospect for rapid fire of very large projectiles (~ 10 rounds/min.)

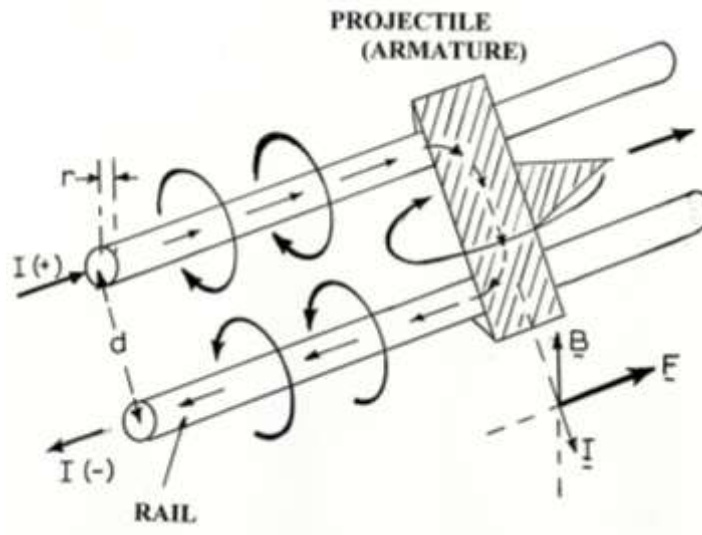


Figure 5.1.1: Schematic view for railgun principles. Current (I) flowing through rails and armature produces surrounding magnetic flux. Armature field interaction with rail flux creates force (F) on the projectile.

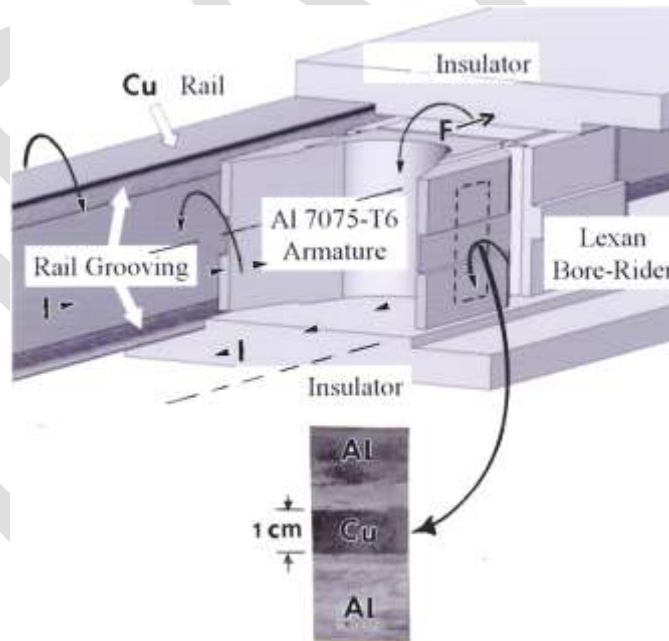


Figure 5.1.2: Section and cut-away view for a railgun system showing armature, rail, and insulator layout in present experiments (after ref. 5). Rail damage on extracted copper rail section is illustrated. Note section reversal. Rail grooving damage occurs at the rail edges. Also note that current, field, and projectile force components are the same as in Fig. 5.1.1.

One of the major contributions to railgun performance limitations has been rail degradation or erosion damage in solid-armature railguns. This is a consequence of projectile (armature) erosion and associated mechanical deformation of the rail surfaces as well as sliding (frictional) and resistive heating, associated melting and so-called plasma erosion (Watt et al 2007). Figure 5.1.2 shows an extracted section of a copper rail following armature (aluminum) erosion deposition, which characterizes the main issue of this study. Similar kinds of damage have also been characterized in high-energy switch electrode and insulator materials comprising high-energy spark-gap switch systems and related pulsed-power applications (Murr et al 1994). Rail damage in railgun systems employing a variety of conductive alloys has been studied by Gee and Persad (2001) while Tzeng (2003) and Meger (2006) have recently summarized railgun material and mechanics research. Related effects such as gauging of rails, armature wear, and liquid metal effects have also been examined (Bourell et al 1999; Stefani and Parker 1999; Persad et al 1989; Persad et al 1997).

In this paper we explore the fundamental microstructural issues associated with aluminum armature-projectile and copper rail degradation using optical metallography, scanning electron microscopy (SEM) and associated energy-dispersive x-ray spectrometry, focused-ion beam characterization methods, and transmission electron microscopy (TEM). The findings confirm and extend previous observations (Watt et al 2007; Gee and Persad 2001; Tzeng 2003; Meger 2006) and point to fundamental materials aspects of sliding friction and wear involving solid-state and melt-phase mechanical or liquid-phase mixing and associated vortex phenomena contributing to dynamic recrystallization and amorphization.

5.2 Experimental Details

Figure 5.1.2 illustrates a section of the railgun test facility utilized in this research program, with an extracted coupon rotated from the inner copper rail surface to the right. Numerous coupons were extracted at various distances along the rail with the features illustrated in Fig. 5.1.2. Examples of these

extracted coupons are shown in Fig. 5.2.1. These coupons do not exhibit the rail grooving features illustrated in Fig. 5.1.2, and this feature was not included in this study. Figure 3 shows typical Vickers microindentation hardness measurements (HV) for these coupons averaged 10 measurements in each coupon location using a digital, instrumental Vickers microhardness tester with a 100 gf load at 10s dwell time. The original copper rail material, in contrast to the extracted coupon in Fig. 5.2.1, exhibited an instrumental Vickers microindentation hardness of 1.6 GPa, or roughly a factor of 3 harder than the tested rail sections in contact with the aluminum-7075 armature (Fig. 5.2.1).

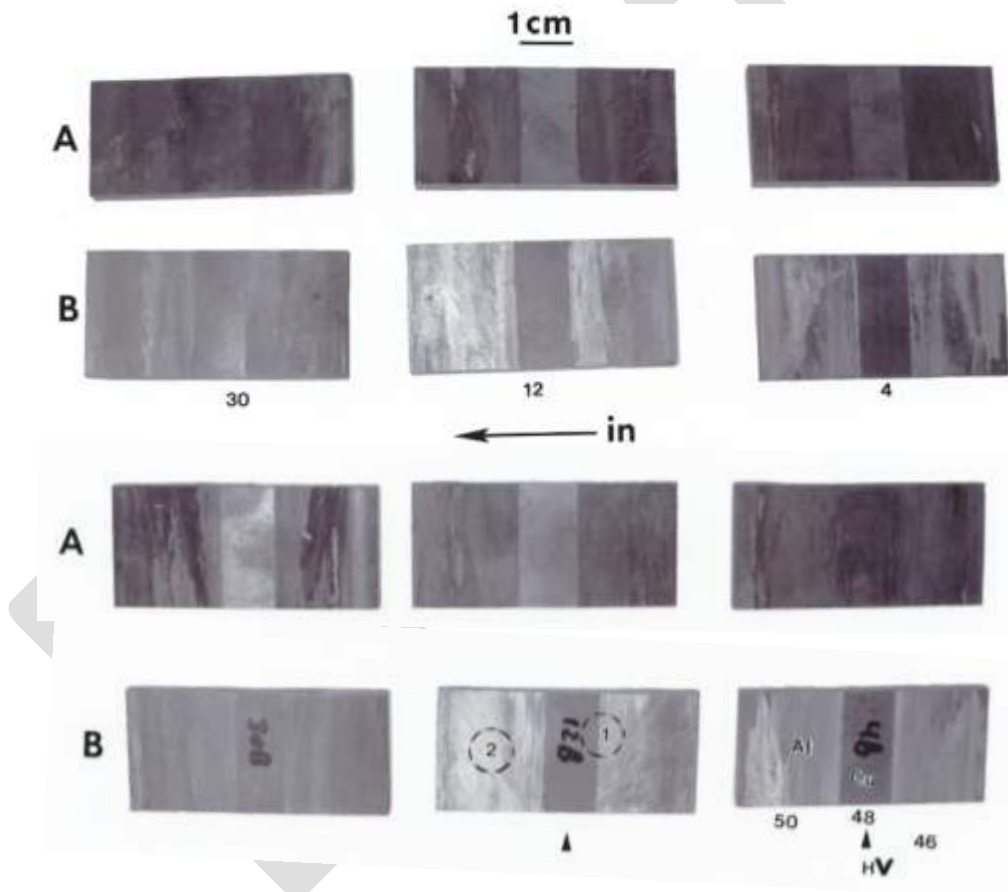


Figure 5.2.1: Examples of left and right (A and B) extracted rail sections as in Fig. 5.1.2 at distances noted (4, 12, and 30 inches (x 2.54 cm/in.). Samples 4B and 12B were examined in detail in this research program. The surface section microindentation hardnesses are shown in the 4B specimen (lower right). Dotted circular enclosures illustrate sample extraction for TEM analysis. 1 refers to electro thinning from the copper side to view through the Al/Cu interface; 2 refers to a region for FIB extraction in order to observe the Al/Cu interface simultaneously (normal to the view for 1).

The extracted coupons (Fig. 5.2.1) were initially examined using scanning electron microscopy in a Hitachi S4800 SEM, operated at 20 kV in the secondary electron emission mode. An EDAX energy-dispersive x-ray spectrometer attachment was also utilized in the examination of the elemental composition of the original copper and aluminum-7075 precursor metals and the extracted coupons (Fig. 5.2.1). Sections from 4A/4B and 30A/30B (Fig. 5.2.1) were cut, mounted, ground, polished and etched; using a solution of 100 mL water, 4 mL sodium chloride, 8 mL sulfuric acid and 2 g potassium dichromate. The etched specimens were observed in three different directions: front, side, top in a Reichart MF4 A/M optical metallograph utilizing a digital image converter. This allowed 3D reconstructions of the microstructure to be developed.

Several sections from 4B and 12B (Fig. 5.2.1) were mechanically thinned from the copper side to the aluminum side (in preparation for TEM observation) to a thickness of ~0.2 mm and punched into 3 mm diameter discs that were electropolished to electron transparency. The electropolishing unit used was a Tenupol 3-dual jet electropolishing unit operated at a polishing current of 0.1 A at a voltage of 8-10 V, using a solution of 825 mL water, 375 mL ethyl alcohol, 300 mL phosphoric acid, 75 mL propanol, and 7.5 g urea at 15°C. The electropolished discs were examined in a high resolution TEM (Hitachi H-9500) operated at 300 kV and utilizing an EDAX attachment for chemical analyses.

Specimens extracted from the copper/aluminum interfacial area (normal to the dashed circle in Fig. 5.2.1 (sample 12b) in the aluminum side) were ion-milled to electron transparency using a Hitachi NB5000 focused ion beam milling machine. The focus ion beam milling machine was operated at a beam current of ~5nA @ 40 kV. It incorporates a high-resolution SEM for imaging the milled sample which when completed is mounted on a special 3 mm holder compatible for viewing in the TEM. Focus ion beam samples were lifted from the copper/aluminum interface so that the interface could be viewed from the perspective shown in Fig. 5.2.1 (sample 12B) at 90° (in the direction of the arrow below the sample 12B in Fig. 5.2.1) below the aluminum erosion film side. This view was normal to the through-

section view examined as described above. Correspondingly, two views of the copper/aluminum interface were prepared in specimens parallel to and normal to the interface.

5.3 Results and Discussion

Figure 5.3.1 shows the copper rail grain structure from the back side of the extracted rail section 12B (arrow) in Fig. 5.2.1. The rail surface section in Fig. 5.3.1 shows somewhat equiaxed, pancake (elongated) grains roughly 5-10 μm in diameter and thicknesses varying from 0.5-2 μm , and some smaller grains. Figure 5.3.2 shows the reverse side (or front side) for specimen 12B shown in Fig. 5.2.1. Figure 5.3.2(a) shows the aluminum, erosion-deposited edge while Fig. 5.3.2(b) shows the center copper region. The aluminum erosion deposit in Fig. 5.3.2(a) shows considerable porosity which is clarified to a greater extent in Fig. 5.3.3(a) and (b) as complex gas bubbles formed in molten aluminum during its deposition resulting from the armature erosion. The aluminum deposition layer composition obtained from the chemical analysis is consistent with the original aluminum-7075 alloy composition (aluminum-zinc-copper), and the copper rail energy-dispersive x-ray spectrum for the exposed copper section in the extracted (12B) sample in Fig. 5.2.1. Figure 5.3.5 illustrates the variation in gas bubble porosity in specimen 4B in Fig. 3 which shows porosity similar to Figs. 5.3.2(a) and (b), and considerably less porosity in the erosion-deposited layer section in Fig. 5.3.4(b) which results by significantly reduced melting. The results illustrated collectively in Figs. 5.3.1(a) and 5.3.2 to 5.3.4 suggest little evidence for conventional alloying of the aluminum/copper overgrowth, and variations in melt propensity for the aluminum deposit, which seems to vary in thickness from ~10-20 μm .

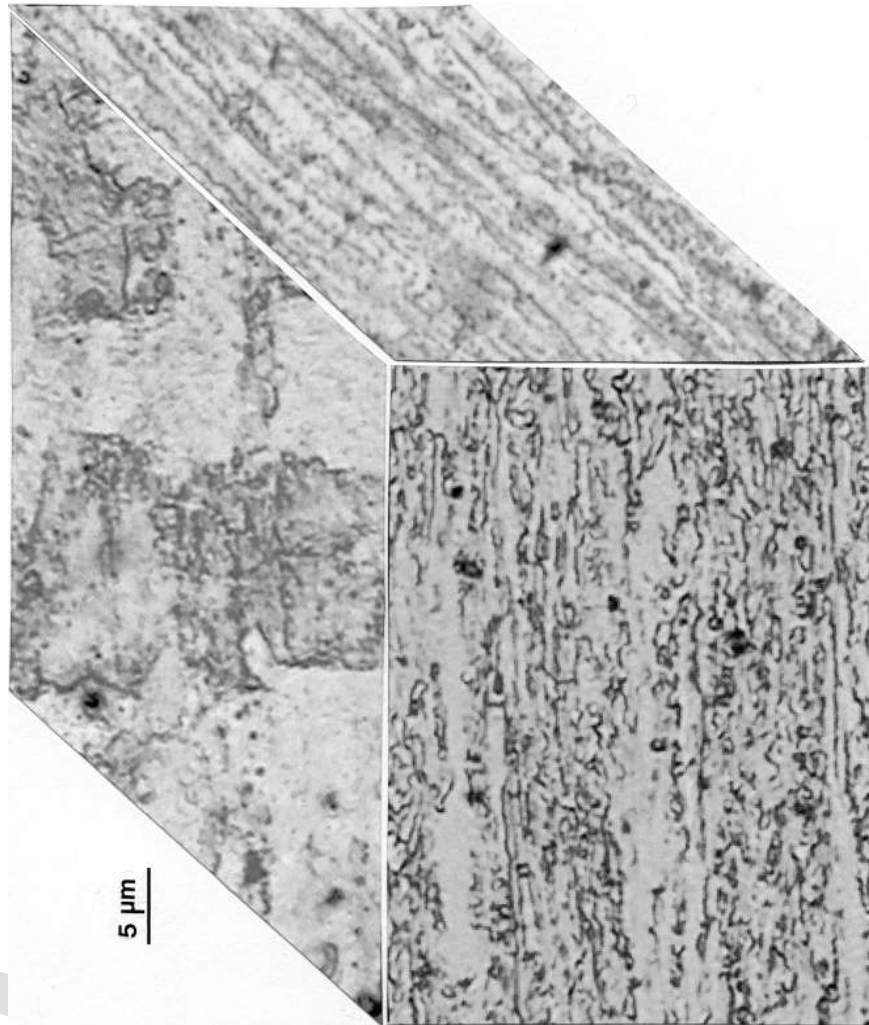


Figure 5.3.1: 3-D optical metallographic composite showing copper rail grain structure to be characterized by thin, irregular pancaked grains.

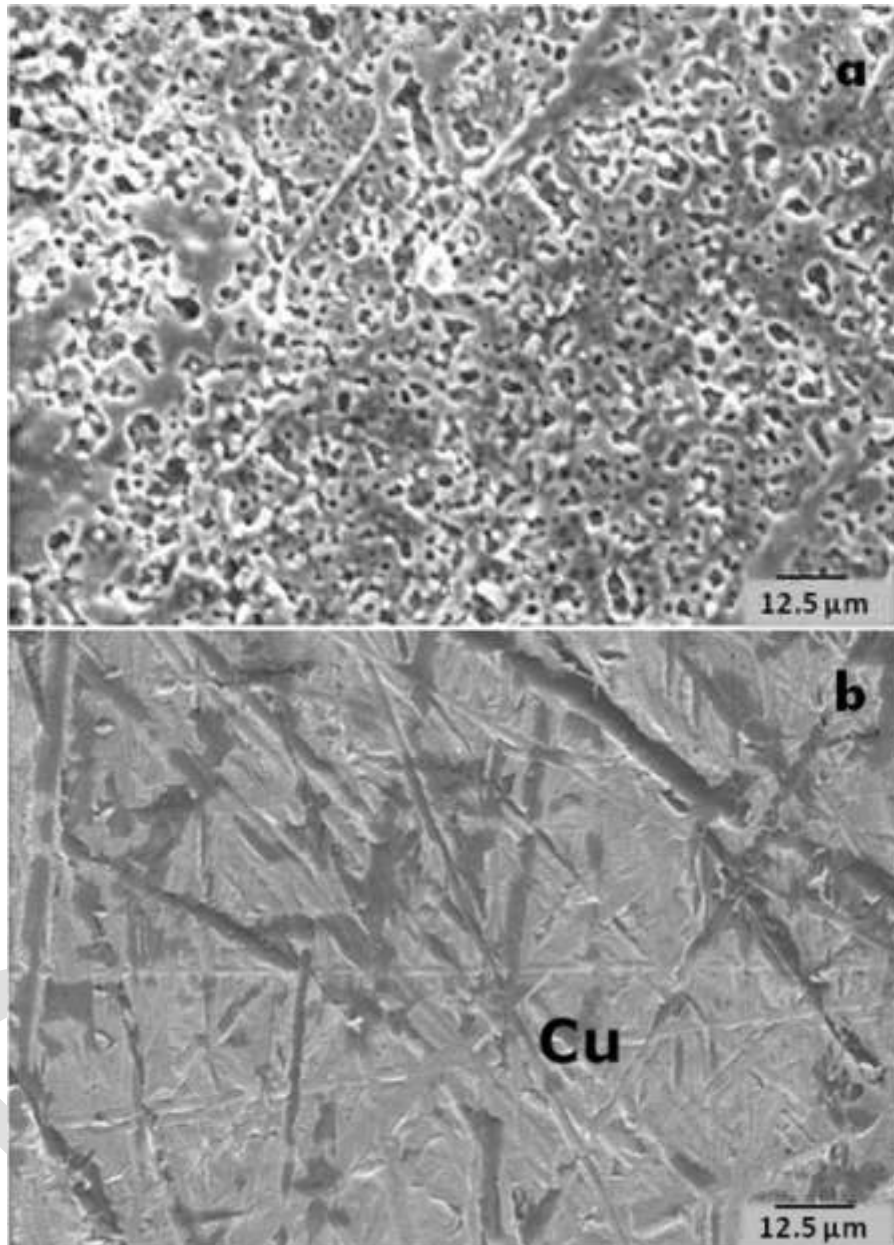


Figure 5.3.2: Al and Cu zone structures in 12B sample (Fig. 3). (a) Porous Al deposit. (b) Scratched Cu rail surface portion. Secondary electron images.

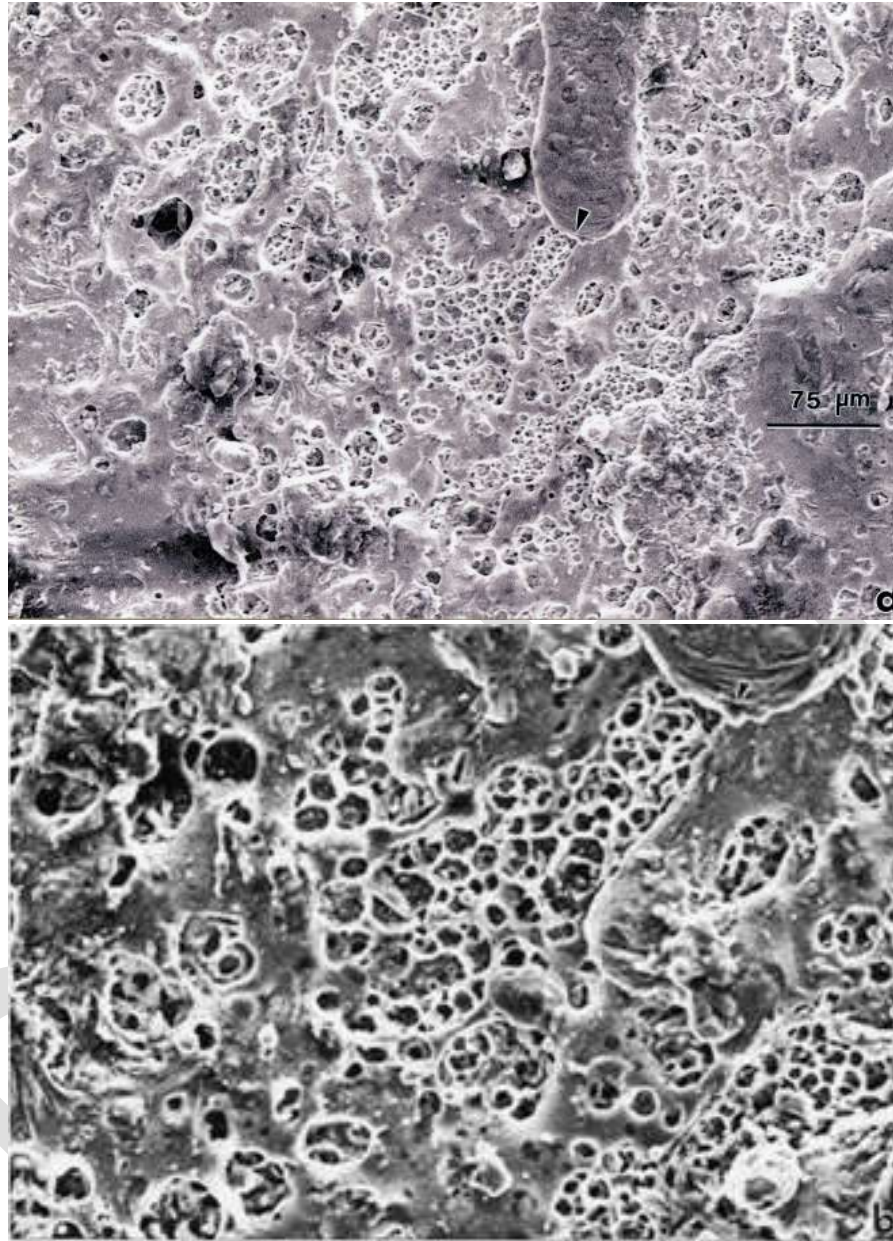


Figure 5.3.3: Low (a) and higher (b) magnification views for porous (gas bubble) structure in Al-alloy projectile, tribomaterial deposit on Cu rail (12B in Fig. 3). Secondary electron SEM images.

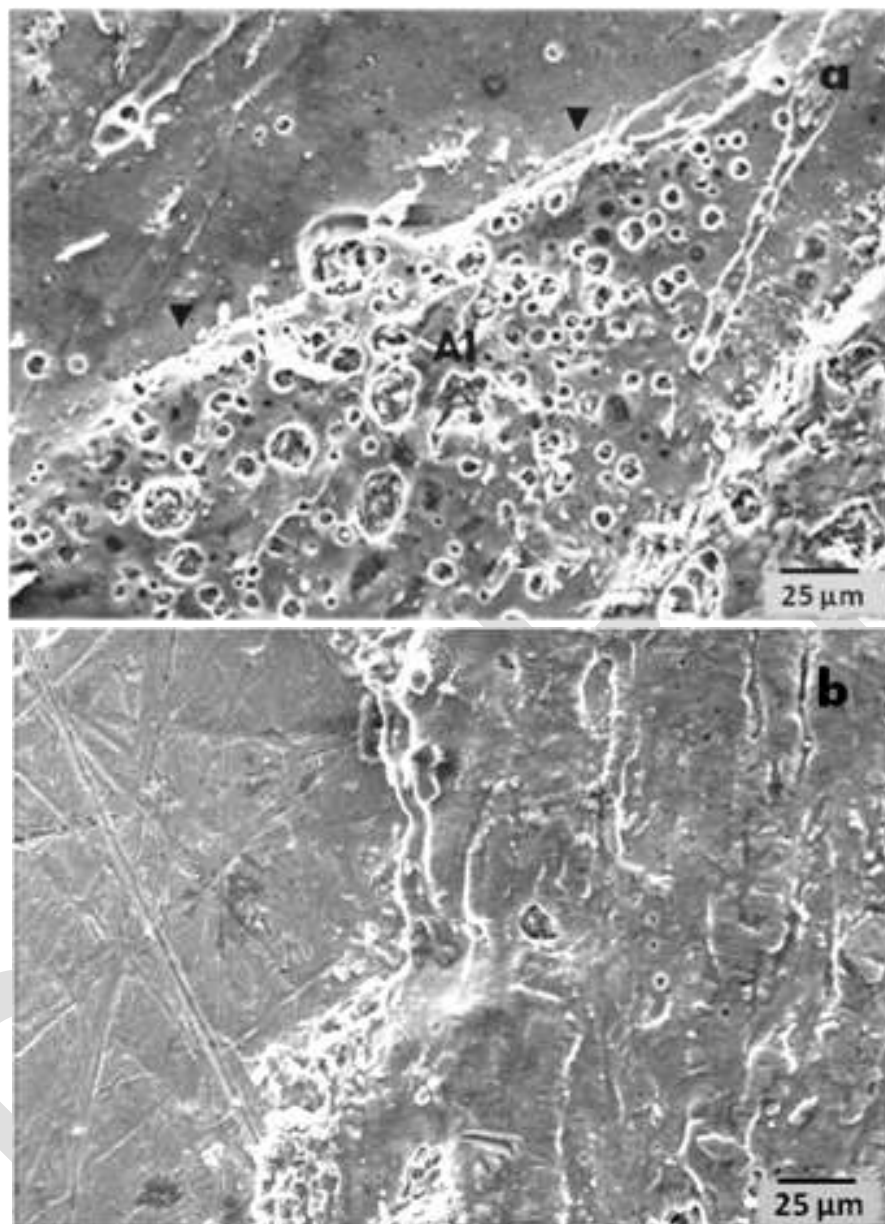


Figure 5.3.4: SEM views showing porosity (gas bubble) variations along the edge of the Al-alloy deposit on the Cu rail. (a) High porosity; (b) low porosity. From sample 4B in Fig.5.2.1.

Thin film specimens prepared at or near the copper rail/aluminum deposit interface region and observed in the TEM consistently illustrated mixtures (mechanical mixing) of copper nanograins, which predominate and aluminum nanograins within an amorphous matrix. These features are illustrated in Fig. 5.3.5. Figure 5.3.5(a) shows prominent, crystalline copper grains (arrows) which vary in size from <50 nm to ~ 500 nm. Since the larger grains are equivalent to the smallest grains in the copper rail (Fig.

5.3.1), these small nano-grains are likely the result of dynamic recrystallization, especially at or very close to the aluminum/copper interface where sliding/contact deformation is highest. These features are also shown in the alternate view of the interfacial region shown in Fig. 5.3.5(b).

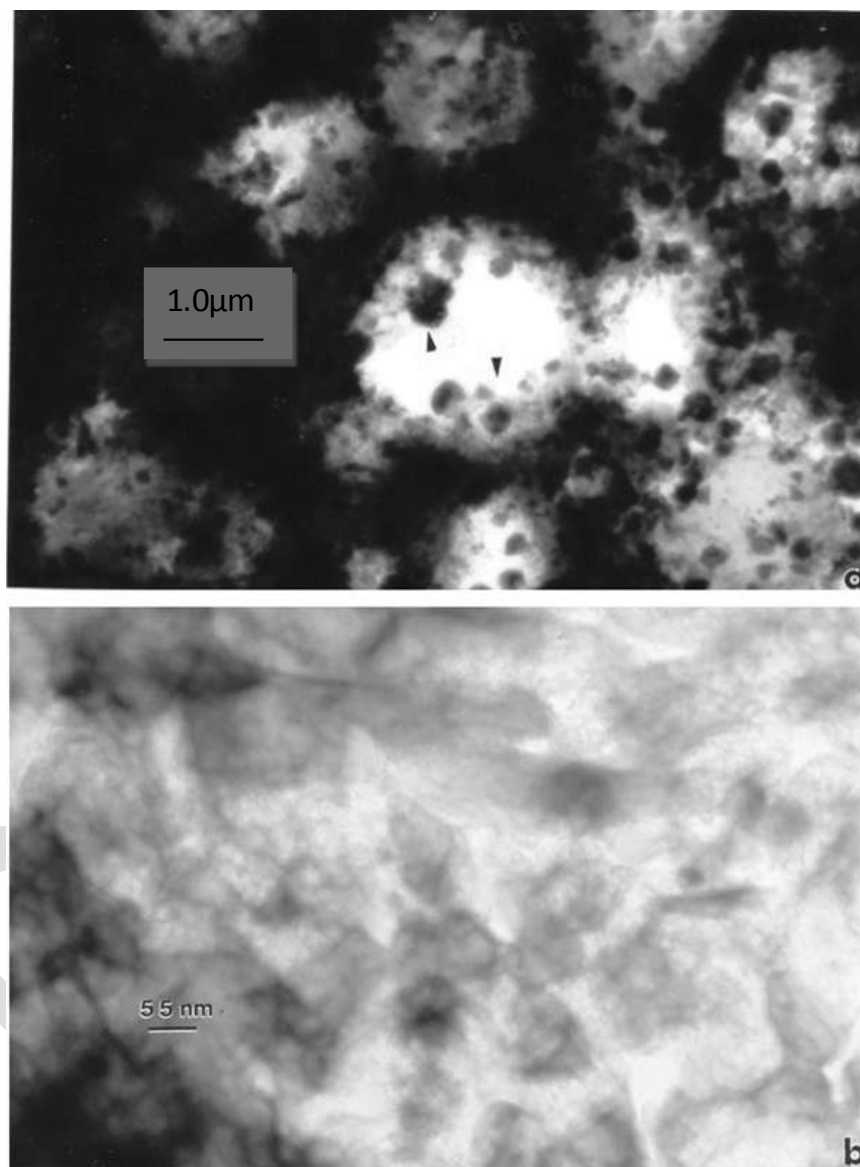


Figure 5.3.5: Corresponding TEM images for thin foil sections representing the Al/Cu interfacial region. (a) Mixing of Cu crystalline grains (arrows) within the Al matrix. (b) crystalline/amorphous mixing: Cu grains in essentially amorphous Al matrix.

Figure 5.3.6 shows two high-resolution TEM views illustrating Moiré fringe features in a thin foil from the interfacial region which confirms the intermixing of very small crystalline grains ranging from ~20 nm to 50 nm within a mostly aluminum matrix. Figure 5.3.7 illustrates a similar, higher-

magnification image in the interfacial aluminum/copper region showing Moiré fringes illustrating simple edge dislocations (arrow) within a crystalline region, corresponding to a dislocation density $\sim 10^{11}/\text{cm}^2$ within the area enclosed by the dotted square, representing ~ 25 nm on a side, and consistent with the apparent grain dimensions in this thin area.

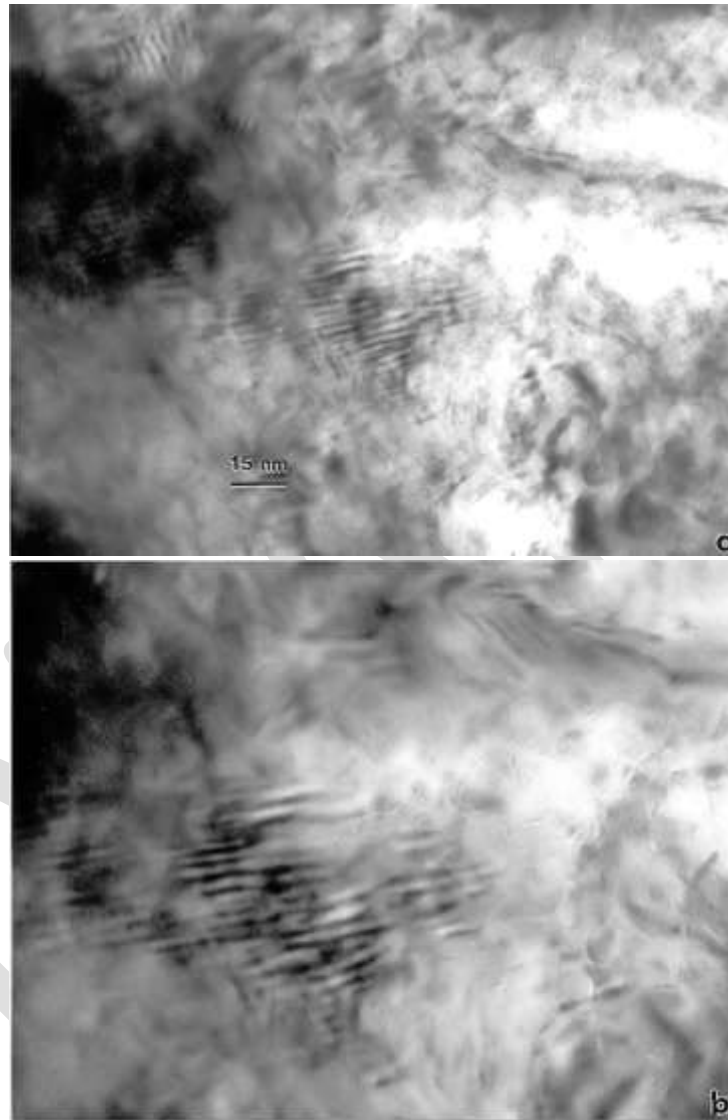


Figure 5.3.6: High-resolution TEM images of Al/Cu interfacial region (12B in Fig. 3) showing Moiré fringe, crystalline features intermixed with amorphous matrix. (a) Low magnification image, (b) higher magnification image.

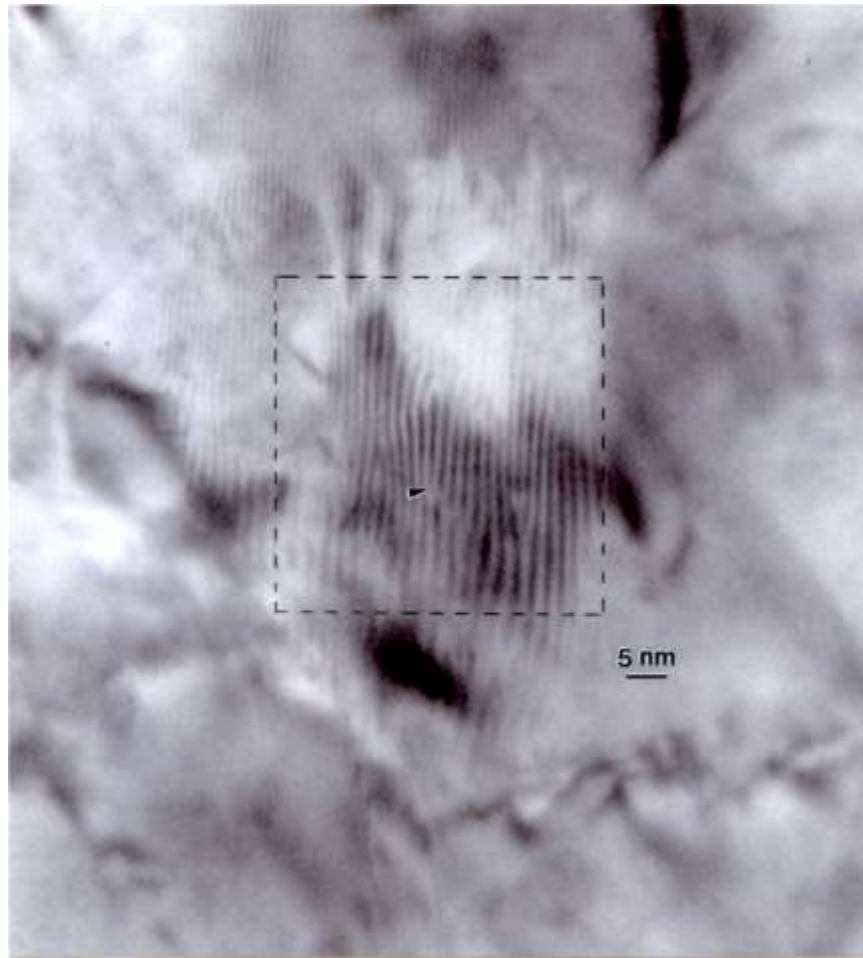


Figure 5.3.7: High-resolution TEM image for crystalline grain showing dislocations (arrow). The dashed-line enclosure represents a reference area 25 nm on a side (625 nm^2).

Figure 5.3.8 shows a region of the copper rail just below the aluminum/copper interface illustrating the irregular grain structure shown in the composite micrograph in Fig. 5.3.1, where the selected-area electron diffraction pattern insert shows a grain boundary misorientation of $\sim 11^\circ$. This structure also shows a dislocation density somewhat lower than Fig. 5.3.7. Taken together, Figs. 5.3.5-5.3.7 provide a consistent comparison differentiating the aluminum/copper interfacial region from the crystalline copper rail microstructure shown in Fig. 5.3.8.

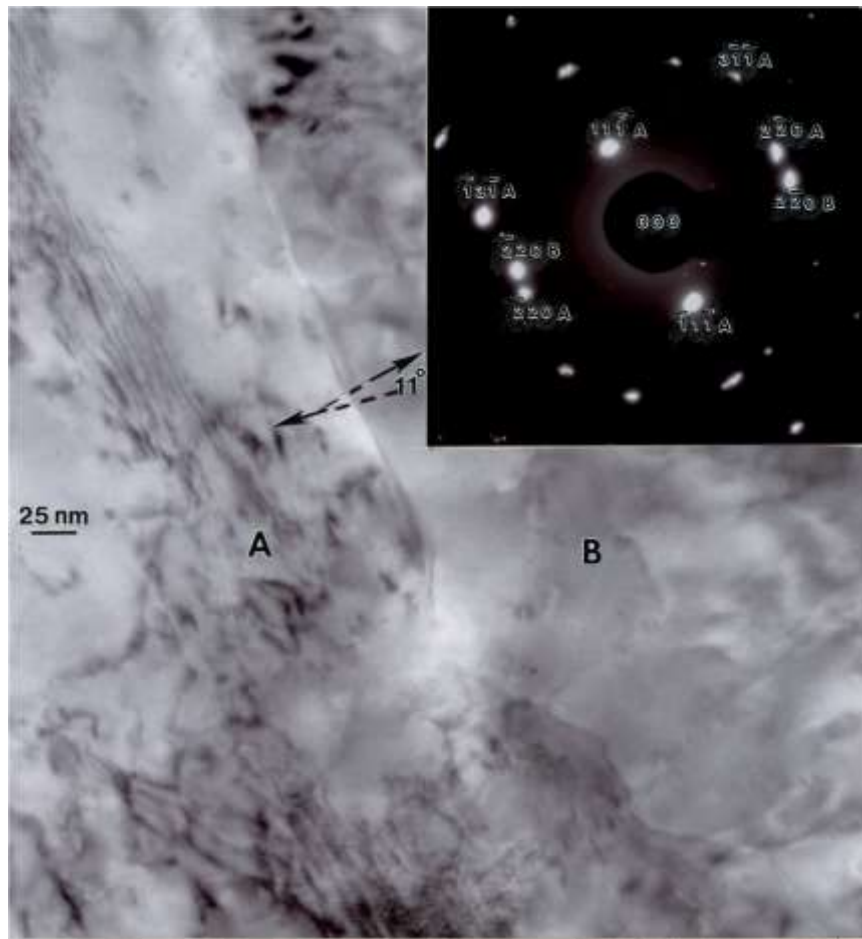


Figure 5.3.8: Near-surface Cu rail microstructure observed in the TEM. The double diffraction spots in the SAED pattern insert attest to the 11° misorientation of the grain boundary. The superimposed patterns for A and B grains each have a (112) surface orientation.

In contrast to the copper/aluminum interface views shown in Figs. 5.3.5-5.3.7, the normal views provided by focus ion beam sections supported the conclusions and implications for these observations. Figure 5.3.9 illustrates a focus ion beam section from the 12B specimen copper/aluminum interface shown in Fig. 5.2.1. The large arrow in the magnified view of the focus ion beam-prepared electron-transparent thin section illustrates a region examined in detail in the TEM as shown in Fig. 5.3.10. Figure 5.3.10 shows, somewhat corresponding to Fig. 5.3.5, the recrystallized grain structure characteristic of both the copper and aluminum sides; with smaller grains and some grain mixing near the transitional (interfacial) region (shown dark in Fig. 5.3.10). While there is some variation in the copper and aluminum regions characterizing the interface in the energy dispersive spectra, the

corresponding x-ray, elemental (aluminum or copper) maps do not indicate any alloying or diffusional phenomena (Figs. 5.3.11(a.) and (b)). Figure 5.3.12 illustrates typical, magnified views for the aluminum and copper (rail) sides of the interfacial bond shown in Fig. 5.3.10. These images correspond to those illustrated in Figs. 5.3.5-5.3.7 especially in support of the ranges of grain sizes. The selected area diffraction pattern insert in Fig. 5.3.12(b) is essentially a template of the selected area diffraction pattern insert in Fig. 5.3.8. However, this spotty copper (face centered cubic) ring pattern corresponds to diffraction from roughly 10 grains, of which 3 are strongly diffracting, and contribute prominent diffraction spots to the ring pattern.

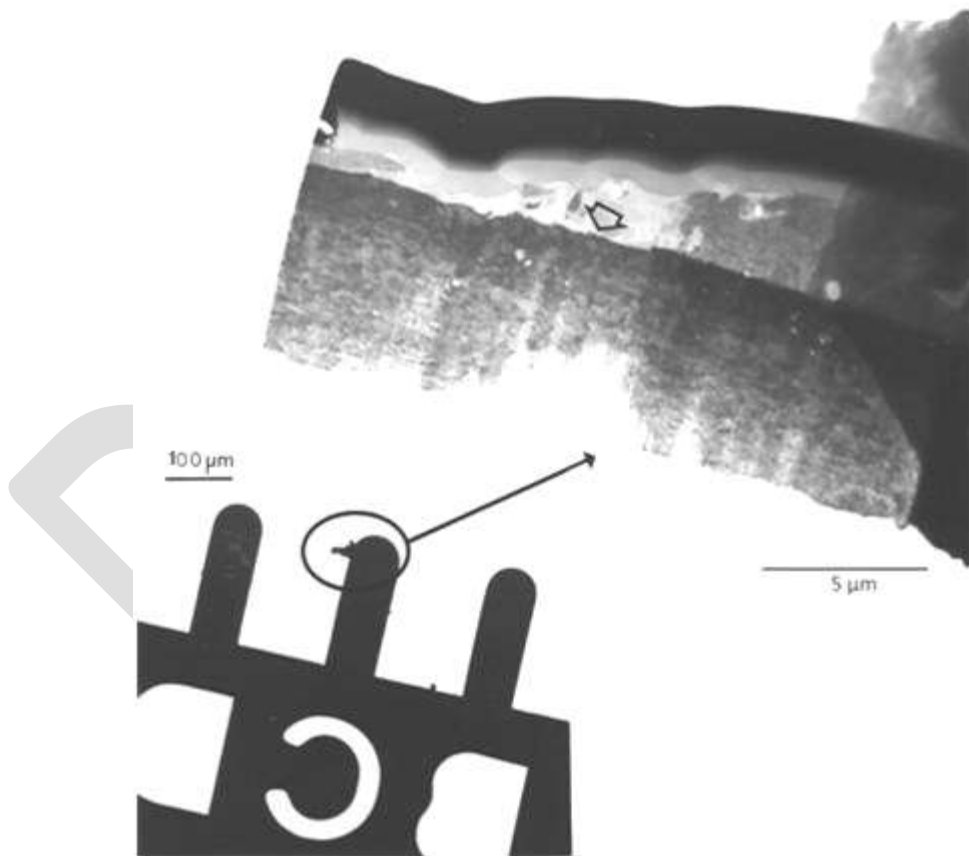


Figure 5.3.9: FIB-prepared and mounted Al/Cu interface section from Fig. 3 (sample 12B). The large arrow in the magnified, TEM-image insert indicates a specific area examined.

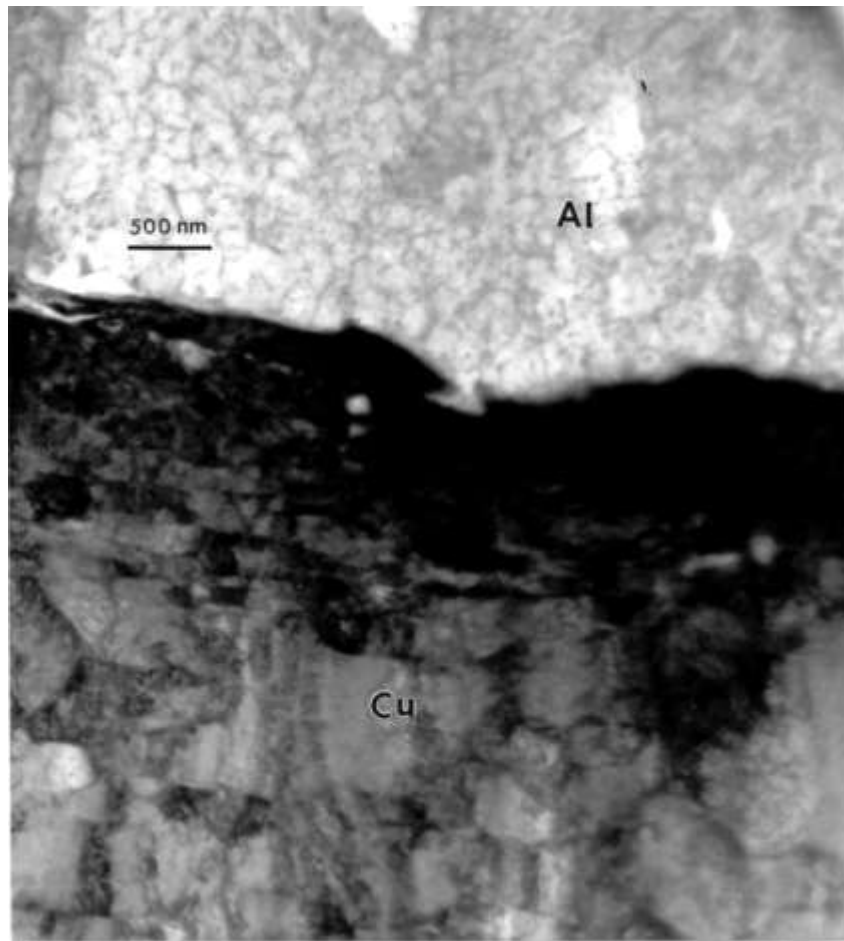


Figure 5.3.10: TEM bright-field image of interfacial Al/Cu region marked by large arrow in Fig. 5.3.9.

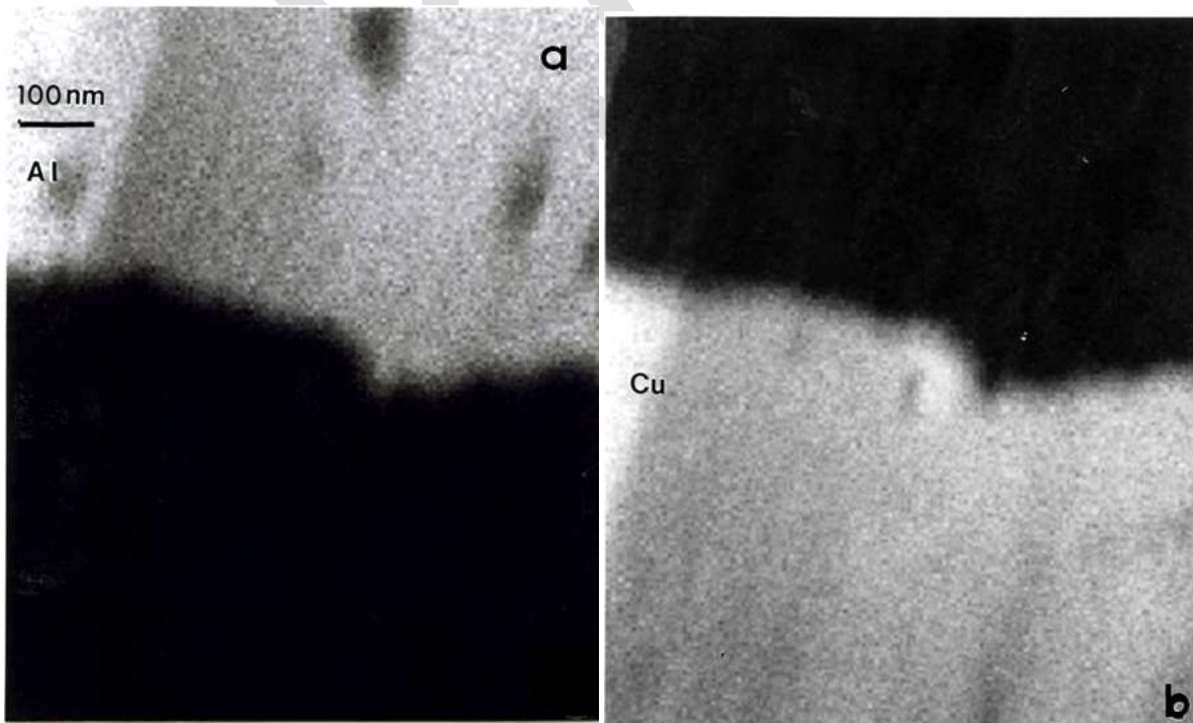


Figure 5.3.11: TEM mapping sequence for the Al/Cu interface in Fig. 13. (a) Al map and (b) Cu map.

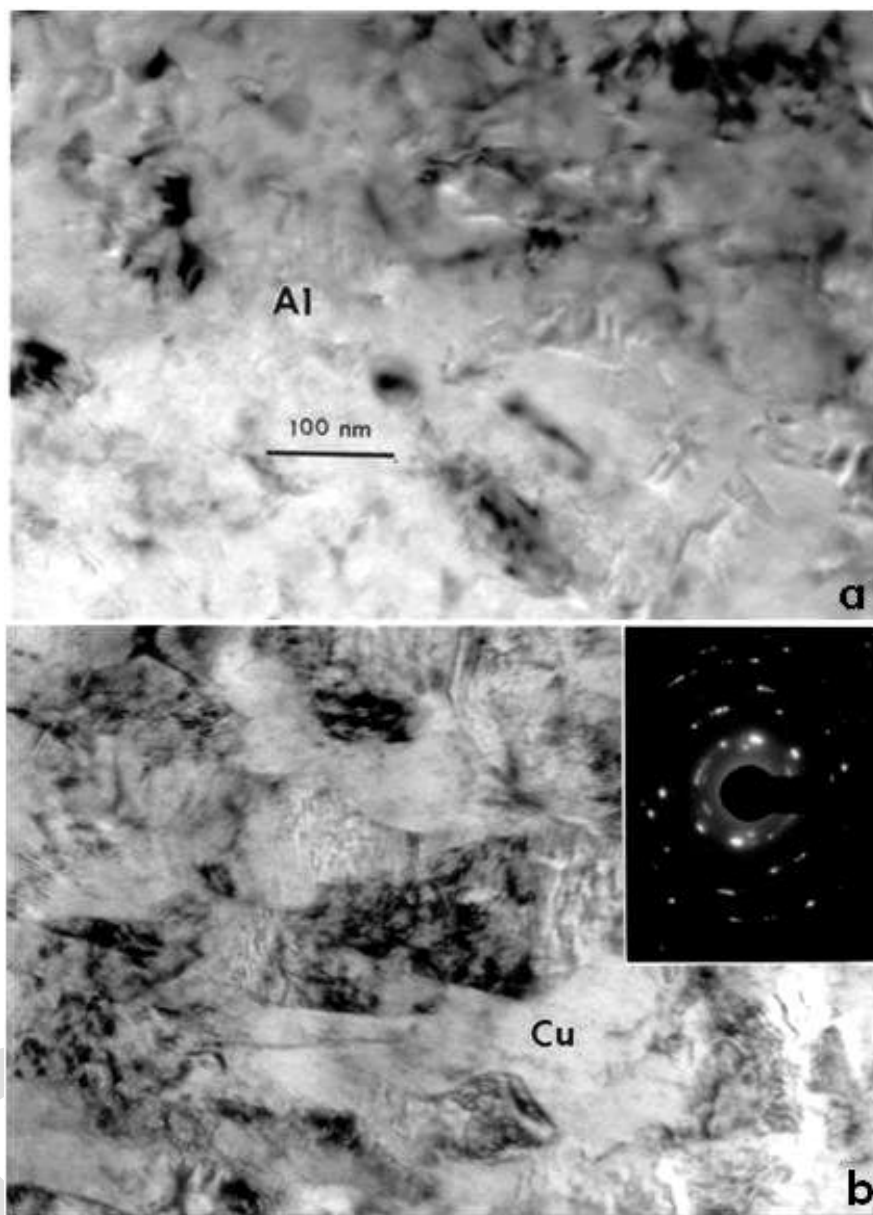


Figure 5.3.12: Magnified TEM images corresponding to Al and Cu regions in Fig. 14 somewhat removed from the interfacial (transitional) region. The SAED pattern insert in the Cu region shows an (fcc) ring pattern.

Retrospectively, the SEM views of the aluminum alloy tribomaterial deposition on the copper rails resulting from sliding friction and wear debris from the armature projectile as shown in Figs. 5.3.2-5.3.4, and the TEM views from the aluminum/copper interfacial region shown in Figs. 5.3.5-5.3.7 and 5.3.10 and 5.3.12, demonstrate the involvement of severe plastic deformation and mechanical mixing contributing to nano-crystalline and/or amorphous tribomaterial, including melting of the aluminum alloy deposit near the surface. These features are consistent with, and partially representative of,

dynamic recrystallization especially prominent for large strains (or deformation) near the contacting surfaces (armature and rail) at high strain rates as a consequence of the projectile velocity. Dynamic recrystallization has been demonstrated to be the dominant mechanism for solid-state flow associated with ballistic projectile/target penetration and interaction (Murr et al 2002; Pizaña et al 2006; Murr et al 2009), friction-stir welding phenomena (Murr et al 1999; Murr 2010), and other high-strain rate deformation phenomena (Murr et al 2007). Friction and wear studies at lower strain rates and severe plastic deformation have also shown dynamic recrystallization to dominate surface-related microstructures, with variations in more conventional microstructures associated with plastic deformation with the stress-strain diagram (such as dislocation or deformation microtwin densities) decreasing with distance from the contacting surface(s). This has been especially prominent for sliding friction and wear phenomena on copper surfaces in the work of Rigney, et al (1986), Karimi et al (1989), and as illustrated more recently by 2-D and 3-D molecular dynamic simulations by Karthikeyan, et al (2009).

In contrast, previous railgun studies have concluded that the dominant mechanism of projectile/rail degradation was erosion by molten aluminum from the armature facilitated by localized electrical heating of the rail (Watt et al 2007), but there is also a contribution from adiabatic heating which occurs coincidentally with dynamic recrystallization and mechanical mixing illustrated in Figs. 5.3.5-5.3.7 and 5.3.10 and 5.3.12. Melting is not a necessary or exclusive feature for tribomaterial flow facilitating sliding and wear, and ballistic rod penetration into thick rolled homogeneous armor steel has been shown to involve melting as a secondary feature in contrast to dynamic recrystallization.

5.4 Conclusions

SEM and TEM studies of the aluminum projectile erosion coating adhering to the copper stator rails in an experimental railgun system indicate a complex interaction involving dynamic recrystallization at the aluminum/copper interface, and melting in the lower temperature aluminum at the

projectile (armature) interface. The dynamic recrystallization was confirmed by TEM observations through the aluminum/copper interface and observations normal to the interface in focus ion beam-prepared specimens. The dynamic recrystallization facilitates material flow, but compromises the rail surface properties when the dynamic recrystallization-erosion coating on tribomaterial deposition occurs. The dynamic recrystallization is characterized by a range of nano-grains by both the aluminum and copper which facilitate mixing and flow at the aluminum/copper interface. There is no evidence for traditional alloying of the aluminum and copper.

Tribomaterial deposition of aluminum armature material on copper rails alters the electromagnetic efficiency and limits railgun performance. However, the fundamental mechanisms contributing to this phenomena, especially dynamic recrystallization, cannot be significantly altered without resorting to a new materials system. This may require a completely new electromagnetic and electrical assessment which may limit performance optimization. In the case of more conventional ballistic projectile penetration into target materials, dynamic recrystallization enhancement improves flow and penetration, but penetration is a singular event. Sustained, discontinuous projectile launch in railguns would, in contrast to similar circumstances where conventional lubrication schemes are utilized, alter the electromagnetic launch efficiency. However, the injection of solid, conducting lubricants, such as graphite, during each launch, may allow for tractable electromagnetic adjustments. It is unclear from this study that any other convenient material substitutions or process modifications will enhance or allow for sustained railgun performance.

5.5 Acknowledgements

This work was supported by the Institute for Advanced Technology, University of Texas – Austin, and the U.S. Army Research Laboratory under Prime Contract No. W911QX-07-D002, Award No. 10-6099. We are also grateful to Jamil J. Clark, Hitachi High Technology America, Ltd. NanoTechnology Systems Group, for providing focus ion beam-prepared specimens for TEM analysis.

5.6 References

- Bourell, D.L., Persad, C. Simulation of railgun gauging. 1999. *IEEE Trans. on Magnetics* 35(1): 274-278.
- Chiltron, F., Hibbs, B., Kolm, H., O'Neill, G., Phillips, J. 1977. Electromagnetic mass driven, Prog. In Astronautics and Aeronautics 57: 37-61.
- Gee, R. M., Persad, C. 2001. The response of different copper alloys as rail contacts at the breach of an electromagnetic launcher. *IEEE Trans. on Magnetics* 37(1): 263-267.
- Karimi, A., Maamouri, M., Martin, J.L. 1989. Cavitation-erosion-induced microstructure in copper single crystals. *Mater. Sci. Eng. A* 113: 287-296.
- Karthikeyan, S., Agarwal, A., Rigney, D.A. 2009. Molecular dynamics simulations of sliding in an Fe-Cu tribopair system. *Wear*, 267, 1166-1173.
- Marshall, R. A. Railgun energy stores and systems. Digest of Technical Papers: 3rd IEEE International Pulsed Power Conference (T. H. Martin and A. H. Guenther, eds.) (1981); IEEE Catalog No. 81CH1662-6, pp. 193-198.
- Meger, R. A. 2006. Railgun materials science. Naval Research Laboratory (NRL) Review: Materials Science and Technology.
- Meger, R. A., Cooper, K., Jones H., Neri, J., Qadri, S., Singer, I. L., Sprague, J., Wahl, K. J. 2005. Analysis of rail surfaces from a multishot gun. *IEEE Trans. on Magnetics* 41(1): 211-213.
- Murr, L.E. 2010. A Review of FSW Research on Dissimilar Metal and Alloy Systems. *J. Mater. Engr. Performance*. 19(8): 1071-1089.
- Murr, L.E., Li, Y., Trillo, E.A., Nowak, B.M., McClure, J.C. 1999. A comparative study of friction-stir welding of aluminum alloys. *Aluminum Trans.* 1(1): 141-154.
- Murr, L.E., Pizana, C. 2007. Dynamic recrystallization: The dynamic deformation regime. *Metall. Mater. Trans. A* 38A(11): 2611-2628.

- Murr, L.E., Ramirez, A.C., Gaytan, S.M., Lopez, M.I., Martinez, E.Y., Hernandez, D.H., Martinez, E. 2009. Microstructure evolution associated with adiabatic shear bands failure in ballistic plug formation in Ti-6Al-4V targets. *Mater. Sci. Engr. A*, 516: 205-216.
- Murr, L.E., Trillo, E.A., Pappu, S., Kennedy, C. 2002. Adiabatic shear bands and examples of their role in severe plastic deformation. *J. Mater. Sci.* 37: 3337-3390.
- Murr, L. E., Williams, F. L., Smith, D. M., Predecki, P., Wang, S-H. A preliminary survey of high-energy switch materials degradation: spectroscopic and microscopic characterization. Digest of Technical Papers: 3rd IEEE International Pulsed Power Conference, *ibid*, pp. 77-84.
- Persad, C., Lund, C.J., Eliezer, Z., Peterson, D.R., Hahne, J., Zowanka, R. 1989. Wear of conductors in rail guns: metallurgical aspects. *IEEE Trans. on Magnetism* 25(1): 221-225.
- Persad, C., Yeoh, A., Prabhu, G., White, G., Eliezer, Z. 1997. On the nature of armature-rail interface: liquid metal effects. *IEEE Trans. on Magnetism* 33(1): 140-145.
- Peterson, Z. M. Record railgun test today. Navy News, Thursday, Jan. 31, 2008.
- Pizaña, C., Murr, L.E., Baquera, M., Anchondo, I.A., Putrevu, A., Peña, C.Y., Tamoria, T.L., Chen, H.C., Cytron, S.T. 2006. Solid-state flow, mechanical alloying, and melt-related phenomena in [001] single-crystal W ballistic rod penetrators interacting with steel targets. *Mater. Sci. Engr. A* 428: 301-313.
- Rigney, D.A., Naylor, M.G.S., Divakar, R., Ives, L.K. 1986. Low energy structures caused by sliding and by particle impact. *Mater. Sci. Eng. A* 81: 409-425.
- Stefani, F., Parker, J. 1999. Experiments to measure wear in aluminum armatures. *IEEE Trans. on Magnetism* 35(1): 100-106.
- Tzeng, J. T. A summary of materials and mechanics research for electromagnetic gun pulsed power applications. 2003. ARL-TR-2948, ARL Report (Army Research Laboratory, Aberdeen, MD).

Watt, T., Stefani, F., Crawford, M., Mark, H., Parker, J. 2007. Investigation of damage to solid-armature railguns at startup. *IEEE Trans. on Magnetics* 43(1): 214-218.

DRAFT

Chapter 6: Summary and Conclusions

6.1 Summary

The two related ballistic nano-particle issues to be studied are therefore: 1. Speciated nano-particles of W, Ni, Co, Fe representing ballistic aerosol examined for human toxicity in comparison to related ballistic aerosol and 2. Railgun erosion of nanoparticulates examined and characterized relative to railgun degradation issues.

6.2 Specific Conclusions

- Nanoparticles of Fe/W; W/Ni; W/Co, etc. exhibit noticeable cytotoxicity but not as significant as the mixture of ballistic aerosol. There is a measurably greater cytotoxicity for the nano powder particulates in contrast to the micron-size particulates
- The characterization of the ballistic aerosol particles in comparison to the commercial (manufactured) powders shows similar morphologies for both the nano and micron size using SEM and TEM analyses
- EDS elemental mapping sequences of the collected ballistic aerosols show that the larger (micron) particles are mainly Fe, but reveal mixtures, of primarily W and Ni composing surrounding nano-size, aggregated particles
- W-Ni-Co or W-Ni-Fe exhibit extreme cytotoxicity and potential for serious health effects, especially short-term and while W is normally not toxic in bulk or micron-size form, nano-W exhibits measurable cytotoxicity.
- Al alloy deposition on the Cu rails resulting from sliding friction and wear debris from the armature-projectile, including melting of the Al near the surface. There is no evidence for traditional alloying of the Al and Cu
- TEM views from the Al/Cu interface demonstrate severe plastic deformation and mechanical mixing contributing to nano-crystalline grains and amorphous matrix which is representative of dynamic recrystallization (DRX)
- A new materials system that may require a completely new electromagnetic and electrical assessment which may limit performance

- The injection of solid, conducting lubricants, during each launch, may allow for tractable electromagnetic adjustments
- It is unclear from this study that any other convenient material substitutions or process modifications will enhance or allow for sustained railgun performance

DRAFT

Curriculum Vita

Brenda Machado was born on February 22, 1984 in Cd. Juarez, Chihuahua, Mexico and is the only child of Jose Luis Machado and Gabriela Lopez. She graduated from Jefferson High School in El Paso, TX, in 2002 as a Valedictorian. She received her Bachelor of Science degree in Metallurgical and Materials Engineering in 2007 from the University of Texas at El Paso (UTEP) and later entered the Graduate School at UTEP to complete her Master of Science (M.S.) degree in Metallurgical and Materials Engineering in December of 2009. Later pursued her Doctoral degree in Materials Science and Engineering interdisciplinary program under the guidance of Dr. Lawrence Murr. During her graduate studies she has worked as a graduate research assistant assisting Dr. Murr with different research projects. As a graduate student she has been supported by the Phelps Dodge Scholarship. She worked as an intern with El Paso Corporation in 2007 and 2009. Her research work has been presented at the Minerals, Metals, and Materials (TMS) Conference, the Materials Science and Technology (MS&T) Conference as well as at the Environmental Research and Public Health Conference and also accepted for publication.

Permanent address: 337 Barcelona Dr.

El Paso, TX 79905

This dissertation was typed by Brenda Machado.